

Characteristics of Kelvin-Helmholtz Waves as Observed by the MMS from September 2015 to March 2020

Rachel Rice¹, Katariina Nykyri¹, Xuanye Ma¹, Brandon Burkholder²

¹Embry-Riddle Aeronautical University, Department of Physical Sciences, Center for Space and Atmospheric Research

²University of Maryland Baltimore County, Goddard Planetary Heliophysics Institute

Key Points:

- A survey of MMS data from September 2015 to March 2020 identified 45 Kelvin-Helmholtz wave events.
- Events are observed for the full range of solar wind conditions. Growth rates are independent of solar wind conditions.
- A new method is developed for the automatic detection of magnetosheath and magnetospheric regions within the KHI.

14 **Abstract**

15 The Magnetospheric Multiscale (MMS) mission has presented a new opportunity to study
 16 the fine scale structures and phenomena of the Earth's magnetosphere, including cross
 17 scale processes associated with the Kelvin-Helmholtz Instability (KHI), but such stud-
 18 ies of the KHI and its secondary processes will require a database of MMS encounters
 19 with Kelvin-Helmholtz (KH) waves. Here we present an overview of 45 MMS observa-
 20 tions of the KHI from September 2015 to March 2020. Growth rates and unstable solid
 21 angles for each of the 45 events were calculated using a new technique to automatically
 22 detect plasma regions on either side of the magnetopause boundary. There was no ap-
 23 parent correlation between solar wind conditions during the KHI and its growth rate and
 24 unstable solid angle, which is not surprising as KH waves were observed downstream of
 25 their source region. We note all KHI were observed for solar wind flow speeds between
 26 295 km/s and 610 km/s, possibly due to a filtering effect of the instability onset crite-
 27 ria and plasma compressibility. Two-dimensional Magnetohydrodynamic (2D MHD) sim-
 28 ulations were compared with two of the observed MMS events. Comparison of the ob-
 29 servations with the 2D MHD simulations indicates that the new region sorting method
 30 is reliable and robust. The ability to automatically detect separate plasma regions on
 31 either side of a moving boundary and determine the KHI growth rate may prove use-
 32 ful for future work identifying and studying secondary processes associated with the KHI.

33 **1 Introduction**

34 The ways in which the solar wind (SW) couples to the Earth's magnetosphere and
 35 its impacts on local space weather are fundamental questions of space physics. Several
 36 mechanisms operating at the magnetopause boundary, such as magnetic reconnection
 37 [Paschmann *et al.*, 1979; Sonnerup *et al.*, 1981; Gosling *et al.*, 1986; Burch and Phan,
 38 2016] and viscous interactions [Axford and Hines, 1961; Otto and Fairfield, 2000; Fair-
 39 field *et al.*, 2000], are responsible for the transfer of mass and energy from the solar wind
 40 to the magnetosphere. Understanding the detailed effects of these processes is vital to
 41 predict and help prevent negative outcomes from space weather. Consider as an exam-
 42 ple, the dawn-dusk asymmetry of the magnetosphere plasma sheet.

43 Observations from Defense Meteorological Satellite Program (DMSP) and Time
 44 History of Events and Macroscale Interactions during Substorm (THEMIS) spacecraft
 45 have established that the cold component ions of the plasma sheet are 30-40% hotter in

46 the dawn flank than in the dusk [Hasegawa *et al.*, 2003; Wing *et al.*, 2005]. Dimmock *et al.*
 47 [2015] conducted a statistical study of the magnetosheath source population as observed
 48 by THEMIS spacecraft over seven years, which showed ions in the dawn flank are on av-
 49 erage 10-15% hotter than those in the dusk flank. This asymmetry is more pronounced
 50 under fast (> 400 km/s) SW conditions [Dimmock *et al.*, 2015]. However, even during
 51 fast SW, the asymmetry of the magnetosheath source plasma is insufficient to produce
 52 the observed asymmetry in the plasma sheet. MHD simulations were unable to repro-
 53 duce the observed sheath asymmetry, but it was apparent in hybrid models, suggesting
 54 a kinetic scale mechanism is responsible for asymmetrically driving the heating of cold
 55 component ions in the sheath [Dimmock *et al.*, 2015].

56 Several physical mechanisms have been proposed as drivers of the observed plasma
 57 sheet asymmetry. The Kelvin-Helmholtz instability (KHI), which occurs regularly at the
 58 magnetopause boundary, is one such mechanism [Otto and Fairfield, 2000; Fairfield *et al.*,
 59 2000; Nykyri *et al.*, 2003; Hasegawa *et al.*, 2004; Nykyri *et al.*, 2006; Taylor *et al.*, 2008;
 60 Foulon *et al.*, 2008; Merkin *et al.*, 2013; Lin *et al.*, 2014; Ma *et al.*, 2014a,b; Nykyri *et al.*,
 61 2017; Ma *et al.*, 2017; Sorathia *et al.*, 2019]. The KHI occurs in regions of large shear
 62 flow [Chandrasekhar, 1961], such as the boundary between the shocked SW (the mag-
 63 netosheath) and the relatively stagnant magnetosphere [Miura and Pritchett, 1982]. Long
 64 established as a source for momentum and energy transport from the SW to the mag-
 65 netosphere [Miura, 1984, 1987], later simulations and observations have shown non-linear
 66 stages of the KHI are also capable of reconnection and mass transport [Nykyri and Otto,
 67 2001, 2004; Nykyri *et al.*, 2006; Hasegawa *et al.*, 2009] and ion heating via kinetic wave
 68 modes within the vortex [Moore *et al.*, 2016, 2017]. Compressional waves, like Kelvin-
 69 Helmholtz or ultra-low frequency (ULF) waves, can also lead to kinetic Alfvén wave (KAW)
 70 generation via mode conversion [Johnson *et al.*, 2001; Chaston *et al.*, 2007]. Recent work
 71 by Nykyri *et al.* [2021] has suggested that KAWs associated with the KHI can contribute
 72 to parallel electron heating, but in that case, were insufficient to account for the total
 73 observed electron heating. Identifying the detailed mechanism or mechanisms driving
 74 electron scale waves within the KHI and quantifying their contribution to electron heat-
 75 ing is still an open question.

76 Observations have shown the KHI may form on both the dawn and dusk flanks un-
 77 der any orientation of the interplanetary magnetic field (IMF) [Kavosi and Reader, 2015],
 78 but simulations have shown a preference for dawn flank formation when the IMF is in

79 a Parker Spiral (PS) orientation [Nykyri, 2013; Adamson *et al.*, 2016]. Work by *Henry*
 80 *et al.* [2017] analyzed the events presented in *Kavosi and Reader* [2015] and confirmed
 81 this preference observationally. *Henry et al.* [2017] also confirmed a preference for KHI
 82 formation at the dusk flank for high solar wind speeds under northward IMF (NIMF).
 83 As PS is the most statistically common IMF orientation, it follows that the associated
 84 preference for dawn-side KHI development would also be statistically more common. Such
 85 asymmetry in the formation of KHI, combined with Kelvin-Helmholtz (KH) driven sec-
 86 ondary processes like reconnection and kinetic scale waves, make the KHI a strong can-
 87 didate to drive the dawn-dusk asymmetry of cold-component ions in the plasma sheet.

88 The launch of the Magnetospheric Multiscale (MMS) satellites presents a new op-
 89 portunity to extend this study of the KHI and its associated secondary processes to smaller
 90 scales with higher resolution measurements. Within months of its launch, MMS had en-
 91 countered KHI [Eriksson *et al.*, 2016]. The event reported by *Eriksson et al.* [2016] has
 92 been the subject of several case studies: *Li et al.* [2016] found evidence of Alfvénic ion
 93 jets and electron mixing due to reconnection at the trailing edge of the vortex; *Wilder*
 94 *et al.* [2016] noted compressed current sheets and evidence of ion-acoustic waves, and *Stawarz*
 95 *et al.* [2016] took advantage of MMS's high temporal and spatial resolutions to study tur-
 96 bulence generated by the KHI. These secondary processes would contribute to ion heat-
 97 ing and plasma transfer across the magnetopause boundary.

98 Case studies are useful in identifying the fine-scale secondary processes associated
 99 with the KHI, but statistical studies are necessary to fully understand their role and quan-
 100 tify their contribution to heating and driving the plasma sheet asymmetry. It is there-
 101 fore imperative, as a first step, to build a database of MMS encounters with KHI. Com-
 102 parison of the location, duration, and prevailing IMF conditions of many events with the
 103 growth rates and unstable solid angles can help establish patterns which may prove in-
 104 formative in understanding the role KHI plays in magnetospheric dynamics (e.g., in gen-
 105 erating dawn-dusk asymmetries via secondary, “cross-scale” processes or affecting the
 106 radiation belt electron populations via ULF wave generation or magnetopause shadow-
 107 ing).

108 In this paper we present a list of MMS encounters with the KHI and the physical
 109 characteristics of each, which may be used for future studies of small scale secondary pro-
 110 cesses. The MMS instrumentation and observational signatures used to identify the KHI

111 encounters are described in Section 2.1 and 2.2, respectively. Growth rates and the un-
 112 stable solid angle used to characterize the KHI are derived in Section 2.3 . Section 2.4
 113 details the methodology used to separate magnetosheath and magnetospheric regions of
 114 the observed events, in order to calculate the growth rates and unstable solid angle for
 115 each event. Results of these calculations are presented in Section 3. The methodology
 116 was also tested using 2-dimensional magnetohydrodynamic simulations as described in
 117 Section 4. Conclusions are presented and discussed in Section 5.

118 **2 Methodology**

119 **2.1 MMS Instrumentation**

120 Observational data reported here is level 2 survey data from MMS1 [*Burch et al.*,
 121 2016]. Spacecraft separations are at most 230 km, and most often between 20 and 50 km,
 122 well below the typical size of the KHI, thus all spacecraft are expected to observe the
 123 same signatures and a single craft is sufficient to identify the KHI. Ion energy spectra
 124 and ion and electron moments are taken from the Fast Plasma Investigation (FPI) [*Pol-*
 125 *lock et al.*, 2016]. The Flux Gate Magnetometer (FGM) provides the DC magnetic field
 126 [*Russell et al.*, 2016; *Torbert et al.*, 2016]. Data file versions used are v3.3.0.cdf for FPI
 127 and v4.18.0.cdf for FGM. SW data are taken from the OMNI database [*King and Pa-*
 128 *pitashvili*, 2005].

129 **2.2 Observational Signatures & Identification of the KHI**

130 Between September 2015 and March 2020, MMS made thousands of full and par-
 131 tial crossings of the magnetopause. In order to narrow the search field, we limited our-
 132 selves to magnetopause crossings which were noted to be unstable in the MMS event database.
 133 Approximately 100 unique intervals were tagged as potentially containing KHI activity.
 134 These crossings were checked by eye to determine if they exhibited the characteristics
 135 of the KHI. These characteristic signatures are as follows:

136 • Quasi-periodic fluctuations in omnidirectional ion energy;

137 When MMS crosses a stable magnetopause boundary, we expect to see a smooth tran-
 138 sition from plasma with energy typical of the magnetosheath to plasma with typical mag-
 139 netospheric energy (or vice versa). When the boundary is not stable, this transition will

140 not be smooth, and may show alternating regions of plasma with energies typical of the
 141 magnetosheath and magnetosphere, as well as mixed energies due to plasma mixing in
 142 the KH vortex. For the case of a boundary disturbed by a periodic instability like the
 143 KHI, these alternating regions should also be relatively periodic.

144

- Quasi-periodic, anti-correlated fluctuations in ion density and temperature;

145 The periodic observation of the magnetosheath and magnetospheric regions will also be
 146 evident in the ion density and temperature, as MMS alternately encounters regions of
 147 plasma from the cold, dense magnetosheath and the hot, tenuous magnetosphere.

148

- Velocity shear(s) on the order of 100s of km/s;

149 Large velocity shears are common at the flank magnetopause, where the magnetosphere
 150 is relatively stagnant and the magnetosheath plasma is accelerating from low speeds im-
 151 mediately after the shock to “catch up” with the SW speed further downtail [Dimmock
 152 and Nykyri, 2013]. Large velocity shears are also a necessary condition for the develop-
 153 ment of the KHI [Chandrasekhar, 1961; Miura, 1984, 1987].

154

- Fluctuations in the total magnetic field;

155 The total strength of the magnetic field will vary as the KH vortex compresses the field
 156 lines.

157

- Bipolar variations in the normal component of the magnetic field

158 Fluctuations in the magnetic field should appear as bipolar variations in the normal com-
 159 ponent as the vortex twists the field lines. Changes in the normal component and to-
 160 tal magnetic field help distinguish the KHI from a shifting boundary, such as a response
 161 to SW dynamic pressure variations.

162

- Fluctuations in total pressure, specifically decreases corresponding to the center
 163 of the KH vortex, where B_N is near 0.

164 The rotational nature of the KHI creates an outward force which is balanced by a pres-
 165 sure gradient, resulting in a decrease of total pressure at the center of the vortex. KHI
 166 events thus show a lower total pressure near the center of the vortex (where B_N is zero)

167 and higher pressure in the spine region. This signature allows us to distinguish the KHI
 168 from a flux transfer event (FTE) in which total pressure typically increases when B_N
 169 is zero [Nykyri *et al.*, 2006; Zhao *et al.*, 2016]. We note that MMS will not always ob-
 170 serve this particular signature, depending on the path MMS takes through the instabil-
 171 ity.

172 Twisting at the boundary is also evident in a comparison of the normal component
 173 with the total bulk velocity. At a quiet boundary, plasma bulk velocity is generally tan-
 174 gential to the boundary. As a KHI twists the boundary, the normal component of the
 175 velocity increases. We compare the maximum absolute value of the normal velocity com-
 176 ponent to the total velocity at the time of observation. For a well developed vortex, the
 177 maximum value of the normal velocity should be a significant fraction of the total ve-
 178 locity. The ratio of the maximum normal velocity to the total velocity for each event is
 179 presented in Section 3

180 To obtain the normal component of the field, observed magnetic field data is ro-
 181 tated into boundary normal (LMN) coordinates using the maximum variance of the elec-
 182 tric field (MVA-E) technique. The general method for variance analysis techniques is given
 183 in Sonnerup and Scheible [1998]. Nykyri *et al.* [2011a,b] showed the single spacecraft MVA-
 184 E technique is sufficient for identification of the boundary normal direction when the plasma
 185 bulk velocity and magnetic field are primarily tangential to the boundary, as is typically
 186 the case during KHI. It is also used here, rather than a multi-spacecraft method, to al-
 187 low for automation of the analysis. For MVA-E, the direction in which the convective
 188 ($\mathbf{v} \times \mathbf{B}$) electric field variance is maximized (i.e., the direction of the maximum eigen-
 189 vector of the variance matrix) is taken as the normal direction, \mathbf{N} . The 180° ambigu-
 190 ity in the normal direction is resolved by requiring the unit normal be positive pointing
 191 outward from the magnetosphere. Tangential directions, \mathbf{L} and \mathbf{M} , are defined by the
 192 intermediate and minimum eigenvectors of the MVA-E matrix, but are not relevant to
 193 the current analysis.

194 All of the above signatures are present in the two example cases shown in Figures
 195 1 and 2. The first five signatures are present in all identified events listed in Table 1. The
 196 final signature is dependent on the MMS trajectory through the KHI, and may or may
 197 not be visible in the observational data for any given event.

198 Figure 1 shows MMS1 survey level observations from 06:00 to 07:00 UT on 15 Oc-
 199 tober 2015, the availability of burst mode data for portions of the interval is indicated
 200 with a blue bar at the top of the figure. MMS passed through the dusk flank of the day-
 201 side magnetopause during strongly duskward IMF. The omni-directional ion energy spec-
 202 trogram in panel (a) shows the expected quasi-periodic variations throughout the inter-
 203 val, which are well matched by anti-correlated changes in ion density and temperature
 204 (c). A velocity shear on the order of 200 km/s is visible near 06:26 UT in panel (d). The
 205 GSM magnetic field in panel (e) shows 20-40 nT fluctuations characteristic of the KHI
 206 from 06:26 to 06:39 UT and again from 06:48 to 06:55 UT. These fluctuations are also
 207 present as bipolar variations in the normal component of the magnetic field (f). Decreases
 208 in total pressure (g) are visible starting around 06:27 UT and continuing through 06:48
 209 UT. The decreases of total pressure correspond with times at which the normal magnetic
 210 field component is near 0, particularly from 06:35-06:40 UT.

217 Survey mode MMS1 observations of another KHI encounter from 16:35 to 19:07
 218 UT on 26 September 2017 are shown in Figure 2. The blue bar at top again indicates
 219 burst mode data is available for portions of the interval. MMS crossed the dusk flank
 220 tail magnetopause while the IMF was in a PS orientation with a strong northward com-
 221 ponent. Quasi-periodic fluctuations in omni directional ion spectra are observable through-
 222 out the interval in panel (a) and are accompanied by anti-correlated variations in ion den-
 223 sity and temperature (c). Velocity shears (d) on the order of 200 km/s occur regularly
 224 throughout the interval. Panel (e) shows fluctuations around 10 nT in the total mag-
 225 netic field, which are also visible as bipolar signatures in the normal component of the
 226 magnetic field (f). Decreases in total pressure (g) of approximately 0.1 nPa correspond
 227 well with times when B_N is near 0.

232 Table 1 summarizes the 45 MMS encounters with the KHI between September 2015
 233 and March 2020. In this time period MMS observed more KH events on the dusk side
 234 magnetopause (29) than on the dawn-side (16). Events are evenly distributed between
 235 the dayside and tail magnetopause: 22 (23) events occur sunward (tailward) of the ter-
 236 minator. KHI in the tail are all observed in or after May 2017, which is primarily due
 237 to a sampling effect of the MMS orbit change from Phase One, which targeted the day-
 238 side magnetopause, to Phase Two, which targeted the tail. The observed events ranged
 239 in duration from as little as 10 minutes to nearly 13 hours. Burst mode data is available

240 for portions of all 45 events, which will be useful for future studies of smaller scale pro-
241 cesses within the KHI.

242 SW data from OMNI is available for 44 of the 45 events, which occur under a va-
243 riety of IMF orientations and solar wind conditions. We consider the planar and B_Z com-
244 ponents separately. At the time at which MMS first observes the KHI, the planar com-
245 ponents of the IMF show a preference for PS (17). Less common are radial, duskward,
246 downward (8 each), and ortho-Parker Spiral (OPS) (3) orientations. For the duration
247 of each event, the planar components of the average IMF configurations show a prefer-
248 ence for the PS orientation (17), followed by radial and downward (8 each) orientations.
249 Duskward (6) and OPS (5) orientations are less common. At the time of first observa-
250 tion, the B_Z component of the IMF was more often northward (27) than southward (17).
251 This preference for NIMF orientation holds true for the duration of each event: 26 (18)
252 of the events occurred under average B_Z positive (negative). The IMF vectors and val-
253 ues of the SW conditions for each event are available in the Supplement. SW parame-
254 ters are discussed and correlated with KHI growth rates in Section 3.

255 Having identified MMS encounters with the KHI, we next calculate the growth rate
256 and unstable solid angle of each event and compare the results with the prevailing so-
257 lar wind and IMF properties.

258 2.3 Instability Growth Rate & Unstable Solid Angle

259 Assuming an infinitely thin boundary layer, a region unstable to the KHI will sat-
260 isfy the KH instability criteria

$$261 [k \cdot (v_1 - v_2)]^2 \geq \frac{n_1 + n_2}{4\pi m_0 n_1 n_2} [(k \cdot B_1)^2 + (k \cdot B_2)^2] \quad (1)$$

262 where v_i , n_i , and B_i are the velocity, density, and magnetic field on either side of the
263 velocity shear layer and k is the wave vector [Chandrasekhar, 1961].

264 Equation 1 may be rearranged to determine the normalized growth rate of the KHI
265 in a particular region, which is defined as

$$266 Q/k = \sqrt{a_1 a_2 (\Delta v \cdot \hat{k})^2 - a_1 (v_{A1} \cdot \hat{k})^2 - a_2 (v_{A2} \cdot \hat{k})^2} \quad (2)$$

267 where a_i is a density parameter for either side of the boundary, defined by $a_i = \rho_i / (\rho_1 +$
268 $\rho_2)$, v_{Ai} is the Alfvén velocity, and \hat{k} is the unit wave vector (thus the growth rate is nor-
269 malized to the wavelength), pointing in the direction of maximum growth. We use only

Table 1. The date, time of first observation, duration, GSM location, and estimated wavelength of 45 KHI events observed by MMS from September 2015 to March 2020. Burst mode data is available for portions of all events.

| Event Number, Date | Onset Time [UT] | Duration [min] | GSM Location [R_E] | KH Wave-length [R_E] | Event Number, Date | Onset Time [UT] | Duration [min] | GSM Location [R_E] | KH Wave-length [R_E] |
|--------------------|-----------------|----------------|------------------------|--------------------------|--------------------|-----------------|----------------|------------------------|--------------------------|
| 01, 08-Sep-15 | 09:00 | 170 | [5.0, 7.4, -4.5] | 2.80 | 24, 19 May-17 | 23:58 | 107 | [-17.8, -16.6, -2.1] | 20.72 |
| 02, 15-Sep-15 | 10:45 | 240 | [5.1, 8.7, -5.5] | 5.00 | 25, 20 May-17 | 02:00 | 150 | [-17.6, -17.4, -0.6] | 26.65 |
| 03, 11-Oct-15 | 10:30 | 30 | [8.7, 6.5, -4.7] | 3.71 | 26, 20 Sep-17 | 22:32 | 43 | [-10.8, 20.9, 1.3] | 8.20 |
| 04, 15-Oct-15 | 06:00 | 60 | [9.0, 4.1, -2.3] | 2.29 | 27, 26 Sep-17 | 16:35 | 152 | [-9.3, 19.6, -0.9] | 6.47 |
| 05, 17-Oct-15 | 16:00 | 28 | [6.4, 7.8, -4.1] | 4.94 | 28, 16 Oct-17 | 14:30 | 50 | [-4.0, 18.6, -2.7] | 7.71 |
| 06, 18-Oct-15 | 15:00 | 25 | [7.2, 7.5, -4.4] | 8.18 | 29, 30 Oct-17 | 19:05 | 35 | [-0.6, 17.3, 1.6] | 4.20 |
| 07, 22-Dec-15 | 22:15 | 35 | [7.9, -5.7, -1.8] | 2.58 | 30, 02 Nov-17 | 17:25 | 50 | [-0.9, 14.8, 0.8] | 6.38 |
| 08, 11-Jan-16 | 20:52 | 18 | [6.2, -7.6, -3.4] | 1.99 | 31, 03 May-18 | 00:15 | 35 | [-9.3, -17.5, -2.3] | 8.43 |
| 09, 19-Jan-16 | 19:57 | 38 | [5.3, -8.2, -3.9] | 3.25 | 32, 18 Sep-18 | 15:50 | 25 | [-14.1, 20.6, -1.0] | 5.17 |
| 10, 05-Feb-16 | 18:55 | 35 | [3.3, -9.3, -5.0] | 5.97 | 33, 24 Sep-18 | 14:10 | 195 | [-14.1, 20.3, -1.6] | 19.35 |
| 11, 07-Feb-16 | 03:45 | 55 | [7.0, -6.9, -3.5] | 4.20 | 34, 02 Oct-18 | 23:45 | 35 | [-10.8, 22.5, 2.1] | 11.25 |
| 12, 18-Feb-16 | 19:30 | 70 | [2.5, -9.7, -6.3] | 6.81 | 35, 04 Oct-18 | 17:25 | 10 | [-0.8, 16.2, -0.2] | 2.50 |
| 13, 25-Feb-16 | 18:55 | 70 | [1.3, -9.9, -6.5] | 2.26 | 36, 13 Apr-19 | 07:45 | 30 | [-0.6, -17.5, 2.4] | 9.68 |
| 14, 26-Sep-16 | 14:15 | 70 | [2.7, 8.5, -5.4] | 11.85 | 37, 03 Jun-19 | 23:05 | 75 | [-2.2, -14.9, -3.8] | 7.46 |
| 15, 27-Sep-16 | 19:50 | 20 | [0.3, 11.5, -3.4] | 2.62 | 38, 25 Sep-19 | 13:45 | 765 | [-16.7, 22.0, -0.2] | 12.33 |
| 16, 04-Oct-16 | 18:20 | 70 | [1.8, 11.2, -3.6] | 9.51 | 39, 02 Oct-19 | 08:15 | 165 | [-9.9, 21.5, -4.5] | 8.54 |
| 17, 10-Oct-16 | 14:40 | 60 | [4.3, 9.3, -5.0] | 9.43 | 40, 02 Oct-19 | 16:00 | 80 | [-12.9, 23.5, -2.1] | 13.03 |
| 18, 24-Oct-16 | 10:50 | 30 | [6.8, 6.1, -4.3] | 1.09 | 41, 02 Oct-19 | 21:40 | 25 | [-14.6, 24.0, 1.1] | 7.11 |
| 19, 04-Nov-16 | 11:45 | 75 | [8.1, 7.2, -3.8] | 2.28 | 42, 06 Oct-19 | 14:50 | 175 | [-14.8, 24.4, -4.2] | 17.10 |
| 20, 03-May-17 | 02:00 | 150 | [-12.9, -19.7, -3.9] | 17.39 | 43, 15 Oct-19 | 19:00 | 75 | [1.2, 12.8, 2.9] | 8.81 |
| 21, 08-May-17 | 13:00 | 110 | [-14.8, -17.2, 0.3] | 11.50 | 44, 22 Oct-19 | 22:00 | 20 | [1.8, 15.3, 3.8] | 3.76 |
| 22, 11-May-17 | 12:00 | 150 | [-15.6, -18.2, 1.4] | 18.47 | 45, 12 Nov-19 | 20:30 | 75 | [6.7, 11.8, 5.2] | 7.04 |
| 23, 11-May-17 | 15:44 | 31 | [-15.3, -19.2, -0.3] | 7.75 | | | | | |

268 proton data to determine the values in Equation 2 as the low mass electrons have no mean-
 269 ingful influence on the growth rate, and minor ion species are not abundant enough to
 270 contribute significantly.

271 Note Equation 2 is an upper limit of the growth rate for an observed event due to
 272 the assumption of an infinitely thin boundary, which is not true for the magnetopause.
 273 Equations 1 and 2 also assume an incompressible plasma, yet for very high (> 600 km/s)
 274 SW speeds, the compressibility is generally sufficient to stabilize the development of the
 275 KHI. Due to these assumptions, the growth rate as determined by Equation 2 is an over-
 276 estimate of the growth rate for an observed KHI. It must also be noted that MMS is un-
 277 likely to observe the source region of the KHI and local conditions may not match those
 278 of the source region. The difference in growth rate from the source region to the obser-
 279 vation point is not predictable from observations.

280 In order to compare the growth rates for KHI events observed at various locations
 281 and under a variety of SW and IMF conditions, we make it unitless via normalization
 282 to the local fast mode speed, $v_{fm} = \sqrt{v_A^2 + c_s^2}$. Both magnetic tension and compress-
 283 ibility have stabilizing effects on the KHI. Likewise, the fast mode speed is dependent
 284 on magnetic tension via the Alfvén velocity, v_A , and compressibility via the sound speed,
 285 c_s . Further, *Miura and Pritchett* [1982] showed the KHI growth rate is strongly corre-
 286 lated to the fast mode speed, and is stable for $Q/k > v_{fm}$, thus it is more physically
 287 meaningful to normalize to the fast mode speed than another characteristic speed.

288 It is also important to note, our expression of the fast mode speed here is an up-
 289 per limit which assumes the magnetic field is perpendicular to the bulk velocity. When
 290 the field and velocity are parallel, the larger of the sound or Alfvén speed is used as the
 291 fast mode speed. This means the unitless growth rate we present is a lower bound, and
 292 may be larger depending upon the relative geometry of the magnetic field and bulk ve-
 293 locity.

The fast mode speed is not equal in the magnetosheath (sub-index *msh*) and mag-
 netosphere (sub-index *msp*), so we normalize to the mean of the two, such that

$$Q_{unitless} = \frac{Q/k}{v_{fm}}$$

294 where $v_{fm} = \frac{1}{2}(v_{fm msh} + v_{fm msp})$.

295 In Equation 2 the direction of $\hat{\mathbf{k}}$ is chosen to maximize the normalized growth rate,
 296 but many directions of $\hat{\mathbf{k}}$ may satisfy the instability criteria. This range of angles capa-
 297 ble of satisfying the instability criteria can be used to determine just how susceptible a
 298 region is to the development of the KHI.

299 The KHI may propagate in any direction $\hat{\mathbf{k}}$ for which Q/k is real (the right hand
 300 side of Equation 2 is positive under the square root). If we express $\hat{\mathbf{k}}$ in terms of the spher-
 301 ical angles ϕ and θ , the percent of the 4π solid angle that satisfies the KHI instability
 302 criteria at a given location may be calculated. We term this percentage the “unstable
 303 solid angle” [Burkholder *et al.*, 2020; Nykyri *et al.*, 2021]. Events with larger unstable
 304 solid angles are likely to be KHI.

305 Growth rate alone is not a sufficient parameter to characterize the KHI; cases with
 306 small growth rates can be indicative of a source region further upstream, such that the
 307 KHI has already created a more diffuse boundary layer. The KHI is a convective insta-
 308 bility which dissipates stored energy as it develops, thus growth rate and the unstable
 309 solid angle are maximized just prior to the formation of the KH vortex. The nature of
 310 in-situ observations, however, dictates we cannot identify a KHI until it is relatively well
 311 developed. Thus small growth rates and unstable solid angles are not necessarily counter-
 312 indicative of the presence of the KHI, but may instead be features of later stage KH waves.

313 As a secondary check for events with low growth rates, we plot tailward velocity
 314 as a function of density to see if the KHI vortex had rolled over, examples of which are
 315 seen in Figure 3. As the KHI develops, it may form non-linear vortices in which low den-
 316 sity magnetospheric plasma becomes trapped and is dragged tailward with magnetosheath-
 317 like velocities. This is seen in observations as low density plasma (typically associated
 318 with the magnetosphere) flowing tailward with the magnetosheath [Hasegawa *et al.*, 2006;
 319 Taylor *et al.*, 2012], and is apparent as points in the lower left quadrant of Figure 3. For
 320 the 15 October 2015 event, ions do not show signatures of roll-over, indicating the KHI
 321 is in an earlier phase of development. For the 26 September 2017 event, ions with magnetosphere-
 322 like density flowing with magnetosheath-like velocities are present, indicating the KHI
 323 has rolled over to form a well-developed vortex.

331 Another indicator of vortex roll-over within the KHI is a comparison of the nor-
 332 mal component with the total bulk velocity. At a quiet boundary, plasma bulk veloc-
 333 ity is generally tangential to the boundary. As a KHI twists the boundary, the normal

334 component of the velocity increases. We compare the maximum absolute value of the
 335 normal velocity component to the total velocity at the time of observation. For a well
 336 developed vortex, the maximum value of the normal velocity should be a significant frac-
 337 tion of the total velocity.

338 Results for the growth rate, unitless growth rate, unstable solid angle, and relative
 339 value of normal velocity are presented in Section 3.

340 **2.4 Automated Region Sorting**

341 Calculation of the growth rate and unstable solid angle requires the identification
 342 of separate regions of magnetosheath and magnetospheric plasma on either side of the
 343 magnetopause boundary. This is made difficult by the plasma mixing inherent within
 344 KH waves. In case studies it is common to select a few minutes of data in the pure mag-
 345 netosheath and magnetosphere regions well away from the unstable boundary area. This
 346 is not, however, the most robust or efficient way to handle region identification for the
 347 many cases necessary for a statistical study. Instead, we seek to automate the process
 348 of separating the magnetosheath and magnetosphere regions.

349 The unperturbed flank magnetosheath is characterized by cold, dense plasma flow-
 350 ing tailward at high speeds with the shocked SW. In contrast the magnetospheric plasma
 351 near the flanks is hot, tenuous, and relatively stagnant. Thus, a combination of density,
 352 temperature, and the X -component of the bulk velocity may be used to separate data
 353 from the magnetosheath and magnetosphere regions. The isolated data provides the mean
 354 values of density, velocity, etc. in each region which are used in the calculation of the
 355 growth rates and unstable solid angle.

356 The magnetosheath is identified by the product of ion density and tailward veloc-
 357 ity divided by the average ion temperature, nv_{tail}/T . The GSM- X velocity component,
 358 v_X , is measured to be large and negative in the sheath and small, either positive or neg-
 359 ative, in the magnetosphere. To simplify our parameter, we shift the tailward velocity
 360 to be strictly positive with a minimum value at 0, such that $v_{tail} = |v_X - \max(v_X)|$.
 361 The resulting parameter, nv_{tail}/T , is thus large in the magnetosheath and small in the
 362 magnetosphere. We identify the sheath as any region in which the value of nv_{tail}/T is
 363 greater than 1.5 times the magnetopause value. The magnetopause value is defined as
 364 the mean of the largest 12.5% and smallest 12.5% of all nv_{tail}/T values (for a total of

365 25% of available data) for each event. This method allows us to reliably identify the mag-
 366 netosheath regions near the KHI while avoiding the inclusion of mixed and transition
 367 regions in our calculations of the KHI growth rate and unstable solid angle (see the Sup-
 368 plementary Information for details justifying the data ranges and cutoff values presented
 369 here).

370 The nv_{tail}/T parameter does not, however, reliably isolate magnetospheric plasma.
 371 Instead, we use the ion specific entropy, $S = T/n^{2/3}$, to identify magnetospheric regions
 372 within each KHI event. The hot, tenuous magnetosphere has much higher specific en-
 373 tropy than the magnetosheath, so we may follow the same procedure as employed for
 374 isolating the magnetosheath with specific entropy in place of the nv_{tail}/T parameter to
 375 separate the magnetosphere. That is, any region with specific entropy 1.5 times greater
 376 than the magnetopause value is considered to be the magnetosphere. Again the mag-
 377 netopause value is the mean of the largest 12.5% and smallest 12.5% (25% total) of all
 378 entropy values for the event. This allows for reliable determination of the magnetospheric
 379 regions near the KHI without including mixed and transition plasma regions (see Sup-
 380 plementary Information).

381 The results of this region sorting method are are depicted in panel b of Figures 1
 382 and 2. Red (blue) bars represent regions of magnetosphere (magnetosheath) plasma. The
 383 green bar identifies regions of mixed plasma. In both example events, the identified re-
 384 gions are in good agreement with omnidirectional ion energy spectrograms and the ion
 385 density and temperature measurements. In Figure 3 red and blue points also represent
 386 the magnetosphere and magnetosheath respectively. In the 2017 case, rolled-over plasma
 387 is considered mixed, despite having density more characteristic of the magnetosphere.
 388 This is a good indicator that our method of automatically separating regions is select-
 389 ing only pure magnetosheath and magnetospheric plasmas and excluding regions where
 390 the KHI has already caused mixing.

391 Having isolated the separate regions, we then calculate mean values of density, tem-
 392 perature, velocity, and magnetic field on either side of the boundary. These values are
 393 checked to ensure they fall within typical ranges for the magnetosheath and magneto-
 394 sphere before they are used in calculation of the growth rate and unstable solid angle.
 395 The new method was also tested using simulation data, and provided good agreement
 396 with known values (see Section 4 and Supplementary Information).

397

3 Observational Results

398 Having separated the magnetosheath and magnetospheric regions of each event,
 399 growth rates (GR), unitless growth rates (UGR), and unstable solid angles (USA) are
 400 calculated. Results for all 45 events are listed in Table 2. GR range from 3.93 to 103.16
 401 km/s. When normalized to the fast mode speed, UGR range from 0.005 to 0.325, but
 402 more typically are between 0.010 and 0.200. That is, the KHI typically develops at 1-
 403 20% of the local fast mode speed; only one event falls below this range and seven above
 404 it. USA range from 0.06 to 39.51%. At its maximum, the normal component of veloc-
 405 ity often accounts for more than 60%, and occasionally all, of the total velocity, indicat-
 406 ing the observed KH waves have significantly twisted the boundary. Events with strongly
 407 twisted boundaries are good candidates for future studies of reconnection and other sec-
 408 onary processes driven by the KHI.

414 GR, UGR, and USA show some dependence on location, as can be seen in Figure
 415 4. The locations of the KHI events observed by MMS are plotted in the GSM X-Y (left
 416 column), X-Z (middle column), and Y-Z (right column) planes and color coded accord-
 417 ing to the GR (top row), UGR (middle row), and USA (bottom row). KHI observed near
 418 the sub-solar point tend to have lower GR than those observed further along the mag-
 419 netopause, particularly those observed along the tail. This is still apparent even when
 420 growth rates are normalized to the local fast mode speeds. This is likely due to the low
 421 velocity shear near the subsolar point. Immediately after the bow shock, the magnetosheath
 422 plasma is slowed significantly from SW speeds, and the shear between the sheath and
 423 magnetosphere is much lower than further downtail, where the magnetosheath plasma
 424 has accelerated and returned to values of SW velocity. The low velocity shear near the
 425 subsolar point will result in lower GR and UGR, as can be seen from Equation 2.

430 USA shows a similar pattern as the GR and UGR, with larger values observed fur-
 431 ther down tail. Again, this can be explained by the large velocity shears encountered along
 432 the tail magnetopause. On the dayside, the shocked solar wind of the magnetosheath is
 433 still accelerating back up to SW speed after encountering the obstacle of earth's mag-
 434 netosphere and bow shock, thus velocity shears between the sheath and magnetosphere
 435 are smaller. Further down tail, the magnetosheath plasma has re-achieved the high SW
 436 flow speed, thus increasing the shear between the two regions. For larger velocity shears,

409 **Table 2.** Growth rates (GR), unitless growth rates (UGR), unstable solid angles (USA), and
 410 the relative value of the maximum normal velocity component for each of the 45 KHI events
 411 observed by MMS from September 2015 to March 2020. At its maximum, the normal velocity
 412 component is a significant fraction of the total velocity for most events. The asterisk indicates
 413 the high-latitude event studied by *Nykyri et al. [2021]* and *Michael et al. [2021]*

| Event Number, Date | GR [km/s] | UGR | USA [%] | v_{Nmax} $/v_{tot}$ | Event Number, Date | GR [km/s] | UGR | USA [%] | v_{Nmax} $/v_{tot}$ |
|-----------------------|--------------|-------|------------|--------------------------|-----------------------|--------------|-------|------------|--------------------------|
| 01, 08-Sep-15 | 81.63 | 0.081 | 6.37 | 0.96 | 24, 19-May-17 | 90.54 | 0.186 | 29.00 | 0.93 |
| 02, 15-Sep-15 | 16.27 | 0.019 | 0.82 | 0.99 | 25, 20-May-17 | 47.42 | 0.066 | 30.22 | 0.75 |
| 03, 11-Oct-15 | 15.68 | 0.016 | 0.42 | 0.58 | 26, 20-Sep-17 | 53.99 | 0.145 | 18.75 | 0.19 |
| 04, 15-Oct-15 | 8.83 | 0.007 | 0.11 | 0.85 | 27, 26-Sep-17 | 52.01 | 0.189 | 24.23 | 0.83 |
| 05, 17-Oct-15 | 25.05 | 0.032 | 4.01 | 0.92 | 28, 16-Oct-17 | 26.03 | 0.047 | 6.74 | 0.79 |
| 06, 18-Oct-15 | 52.31 | 0.063 | 9.07 | 0.83 | 29, 30-Oct-17 | 11.51 | 0.023 | 4.70 | 0.97 |
| 07, 22-Dec-15 | 10.41 | 0.010 | 0.29 | 0.83 | 30, 02-Nov-17 | 39.55 | 0.109 | 5.95 | 0.67 |
| 08, 11-Jan-16 | 17.47 | 0.015 | 0.27 | 0.89 | 31, 03-May-18 | 95.59 | 0.325 | 23.37 | 0.97 |
| 09, 19-Jan-16 | 13.78 | 0.025 | 0.12 | 0.52 | 32, 18-Sep-18 | 40.87 | 0.090 | 9.96 | 0.91 |
| 10, 05-Feb-16 | 22.31 | 0.028 | 5.74 | 0.93 | 33, 24-Sep-18 | 71.16 | 0.227 | 36.91 | 0.73 |
| 11, 07-Feb-16 | 13.36 | 0.019 | 0.16 | 0.66 | 34, 02-Oct-18 | 41.17 | 0.111 | 10.18 | 0.65 |
| 12, 18-Feb-16 | 34.90 | 0.038 | 8.96 | 1.00 | 35, 04-Oct-18 | 31.26 | 0.081 | 6.16 | 0.50 |
| 13, 25-Feb-16* | 5.01 | 0.012 | 0.08 | 0.69 | 36, 13-Apr-19 | 48.93 | 0.089 | 15.66 | 0.76 |
| 14, 26-Sep-16 | 51.46 | 0.068 | 7.26 | 0.99 | 37, 03-Jun-19 | 42.25 | 0.108 | 16.63 | 0.94 |
| 15, 27-Sep-16 | 84.07 | 0.117 | 8.37 | 0.96 | 38, 25-Sep-19 | 74.22 | 0.198 | 28.04 | 0.91 |
| 16, 04-Oct-16 | 54.67 | 0.063 | 7.17 | 0.70 | 39, 02-Oct-19 | 29.28 | 0.083 | 6.10 | 0.58 |
| 17, 10-Oct-16 | 43.30 | 0.059 | 8.98 | 0.75 | 40, 02-Oct-19 | 96.46 | 0.209 | 26.71 | 0.82 |
| 18, 24-Oct-16 | 3.93 | 0.005 | 0.06 | 0.71 | 41, 02-Oct-19 | 37.12 | 0.111 | 18.09 | 0.52 |
| 19, 04-Nov-16 | 16.78 | 0.019 | 0.78 | 0.95 | 42, 06-Oct-19 | 82.43 | 0.210 | 34.49 | 0.98 |
| 20, 03-May-17 | 56.65 | 0.197 | 39.51 | 0.85 | 43, 15-Oct-19 | 94.08 | 0.296 | 18.37 | 0.98 |
| 21, 08-May-17 | 84.15 | 0.278 | 29.87 | 1.00 | 44, 22-Oct-19 | 52.52 | 0.110 | 12.00 | 1.00 |
| 22, 11-May-17 | 45.56 | 0.103 | 12.07 | 0.87 | 45, 12-Nov-19 | 103.16 | 0.250 | 14.34 | 0.90 |
| 23, 11-May-17 | 49.99 | 0.198 | 13.33 | 0.33 | | | | | |

437 the stabilizing effects of the magnetic field are less influential in the development of KHI,
 438 and a larger solid angle is thus unstable to the growth of the KHI.

439 A cluster of KHI events occur at high southern magnetic latitudes ($\text{GSM-Z} < -4.5R_E$),
 440 showing the KHI is not limited to lower latitudes. This is a new finding, as previous mis-
 441 sions, such as THEMIS, remained at lower magnetic latitudes. Only three prior stud-
 442 ies, two using Cluster data [Hwang *et al.*, 2012; Ma *et al.*, 2016], and one using MMS data
 443 [Nykyri *et al.*, 2021; Michael *et al.*, 2021] (marked with asterisk in Table 2), have been
 444 conducted on the KHI at high latitudes near the dawn and dusk flanks of the high-altitude
 445 cusps.

446 Figure 5 depicts the GR (top), UGR (middle), and USA (bottom), of 44 of the 45
 447 events as a function of SW density (far left), temperature (center left), flow speed (cen-
 448 ter), Alfvén Mach number (center right), and IMF magnitude (far right) taken from OMNI
 449 data. OMNI data was not available for one event. The color bar indicates the event num-
 450 ber, so each event is shown with the same color in all plots for direct comparison.

451 SW density ranges from 2.6 to 17.0 /cc. Observed events are well distributed over
 452 the density range, and no relationship is apparent between density and GR or USA. Tem-
 453 peratures generally range from 0.7 to 31.4 eV, with one outlier event occurring with a
 454 SW temperature of 61.0 eV. Most events are observed for SW temperatures less than
 455 20 eV, but no trend in GR, UGR, or USA is apparent.

456 There is an apparent selection window in the solar wind flow speed, with all events
 457 occurring when solar wind flow is between 295 and 610 km/s. This fits with expectations
 458 that low velocity shears between the sheath and magnetosphere are not unstable to the
 459 KHI, and compressibility effects for very large shears stabilize the KHI [Miura and Pritch-
 460 ett, 1982]. Within this selection window there is no correlation between SW flow speed
 461 and GR, UGR, or USA. Alfvén Mach numbers also show no clear relationship to GR,
 462 UGR, or USA. Events are observed for Alfvén Mach numbers between 3.8 and 26.3, though
 463 most events occur when the Mach Number is below 20.

464 IMF magnitude for all but one event is greater than 1.5 nT and less than 11.2 nT.
 465 The outlier event occurred for an average IMF magnitude of 20.8 nT [Eriksson *et al.*,
 466 2016]. Events are otherwise evenly distributed throughout the range of IMF magnitudes
 467 with no apparent relationship to GR, UGR or USA.

468 We also compare the solar wind conditions for which KHI is observed to the so-
 469 lar wind conditions throughout the entire 4.5 year interval from September 2015 to March
 470 2020 in Figure 6. MMS observes KHI for the full range of solar wind conditions. Den-
 471 sity, temperature, flow speed, and Alfvén Mach number values during KH intervals oc-
 472 cur with similar frequency as in the full time range with only slight deviations. The most
 473 pronounced difference is in SW flow speed. KHI intervals overrepresent high SW speeds,
 474 particularly between 350 and 450 km/s. This is unsurprising, as KH develop preferen-
 475 tially for high (> 400 km/s) SW speeds and compressibility at very high speeds (> 600
 476 km/s) can have a stabilizing effect. Given the distribution of SW speeds during the 4.5
 477 year interval, the apparent selection window in SW speed is probably not significant, as
 478 the solar wind speed is not often below 300 km/s or above 600 km/s.

483 As can be seen in Figure 7, IMF magnitude during KH intervals is nearly identi-
 484 cal to the observations in the complete time range, with a small decrease around the most
 485 common strength and an increase at very large IMF (this is due to the outlier event oc-
 486 curring for $\text{IMF} \approx 20$ nT [Eriksson *et al.*, 2016]). The planar IMF components show no
 487 significant or conclusive variation from the full time range to the KHI intervals. For the
 488 B_Z component of the IMF, KHI intervals tend to occur more for NIMF than southward
 489 IMF (SIMF). This is likely due to subsolar reconnection during SIMF, which creates a
 490 more diffuse boundary layer which is less prone to the development of the KHI.

494 The SW conditions and IMF orientations help explain the observation of more KHI
 495 on the dusk side of the magnetopause than on the dawn side. *Henry et al.* [2017] found
 496 dusk flank formation to be more common both for high SW speeds (> 400 km/s) and
 497 NIMF orientations. 25 of the 45 events occur when SW speed was high, and 29 of the
 498 45 events had IMF orientations with positive B_Z components.

499 4 Comparison with Simulations

500 To verify our method of isolating regions on either side of the boundary is robust,
 501 it was applied to parameters generated by two dimensional MHD simulations of the KHI.
 502 A simulation case for a KHI developing under NIMF conditions was tested using initial
 503 conditions comparable to those of the event on 08 September 2015. A second simulation
 504 case used initial conditions similar to those of the 18 October 2015 event for the KHI
 505 developing under Parker Spiral IMF (PSIMF) orientation.

506 The simulations, after *Ma et al.* [2019], solve the full set of resistive Hall-MHD equa-
 507 tions using a leapfrog scheme [Potter, 1973; Birn, 1980; Otto, 1990]. We normalize all
 508 physical quantities to their typical scale, for example, the length L is normalized to L_0 ,
 509 the half width of the initial sheared flow; number density to n_0 , the magnetic field to B_0 ,
 510 velocity to the Alfvén velocity, $v_A = B/\sqrt{\mu_0\rho_0}$; and the time to the Alfvén transit time
 511 $T_A = L_0/v_A$. Exact values of the normalizations for both simulation cases are listed
 512 in the Supplement.

513 A cut is taken through the simulation box at every time step. Data from these cuts
 514 are separated into distinct regions using the method described in Section 2.4, then used
 515 to calculate GR and USA. The GR as a function of time is shown in blue in panel (a)
 516 of Figures 8 and 9 for the NIMF and PSIMF cases respectively. The GR of the obser-
 517 vation case on which the simulations are based is also shown in black, and the simula-
 518 tion GR is shown in green. The simulation GR is determined using a plot of the natu-
 519 ral logarithm of the maximum velocity component perpendicular to the boundary within
 520 the simulation, $\ln(v_{\perp max})$, as a function of time. Such plots have an initially linear por-
 521 tion before leveling off at a near constant value. The slope of the linear portion is the
 522 simulation GR. The development of the KHI is shown in panels (b)-(f), which depict den-
 523 sity at several time steps throughout the simulation. The cuts used for calculations are
 524 shown in red in the same panels.

535 As can be seen in Figures 8 and 9, the KHI growth rate increased from its initial
 536 value until the cut through the simulation captured vortex roll-over. After roll-over is
 537 observed, growth rate decreases sharply then increases towards its initial level as the in-
 538 stability dissipates. All of this is consistent with expectations: the free energy available
 539 to drive the KHI peaks before the vortex forms. The KHI then dissipates the energy.

540 In the NIMF case, GR calculated using Equation 2 are significantly greater than
 541 the simulation GR. This is to be expected as Equation 2 assumes an infinitely thin bound-
 542 ary layer and incompressible plasma; the simulation GR is free from these assumptions.
 543 In contrast, the simulation GR is larger than, though very near, the GR determined us-
 544 ing Equation 2 for the PSIMF case. This may be due to other assumptions made in the
 545 simulation (e.g. pressure is not constant, beta is smaller than observed).

546 Within the first few time steps, the simulation matches well with the observed GR
 547 for the NIMF case. The GR of the event the NIMF simulation is based on is 81.63 km/s.

548 The initial GR for the simulation is 82.74 km/s, and remains within 5 km/s of the ob-
 549 served GR for more than 80 time steps. That is, the first 20% of the simulation is in rough
 550 agreement with the observation.

551 The PSIMF simulation shows equally good, if not better, agreement with the ob-
 552 served event on which it is based. The observed event has a GR of 52.41 km/s, and the
 553 initial GR value for the simulation is 52.44 km/s. The GR of the simulation remains within
 554 5 km/s of the observation's GR for more than 230 time steps, or nearly 60% of the sim-
 555 ulation.

556 We note the growth rate is dependent upon the geometry of the cut. The method
 557 of separating the two regions works best when the spacecraft spends a significant por-
 558 tion of the event duration on both sides of the boundary. Therefore, events in which MMS
 559 only skims the KHI or spends significantly more time in one region than the other may
 560 actually grow faster than our calculations would indicate. The dependence of GR on cut
 561 geometry is discussed in more detail in the Supplementary Information.

562 5 Conclusions and Discussion

563 The main conclusions may be summarized as follows:

564 • MMS observed 45 clear KHI events from September 2015 to March 2020.

565 From September 2015 to March 2020 MMS observed more than 100 unique mixed
 566 regions which initially resembled the KHI. Further analysis of total pressure and boundary-
 567 normal rotated magnetic field showed 45 of these events likely to be the KHI. These 45
 568 events, summarized in Table 1, occur under a variety of prevailing SW conditions and
 569 IMF orientations.

570 The 45 events presented here form the beginnings of a database for statistical stud-
 571 ies of the KHI and its associated secondary processes. Burst mode data is available for
 572 portions of all the identified events. This is useful and necessary for future studies of sec-
 573 ondary processes approaching the electron scale. The methods used here may also be
 574 applied to the MMS data from April 2020 to present to further extend the database of
 575 events for analysis.

576 • An automated method uses nv_{tail}/T and specific entropy to identify the magne-
 577 toshéath and magnetospheric regions, respectively, within a KH wave event. This
 578 method consistently isolates the pure regions, and excludes mixed plasma, both
 579 for real satellite and simulated data.

580 The identified magnetosheath and magnetospheric regions of each KHI event match
 581 well with the omni-directional ion energy spectrogram and density and temperature time
 582 series. Mean values of density, temperature, velocity, and magnetic field in the identi-
 583 fied regions are consistent with expectations. Plots of the GSM- X velocity and density
 584 show mixed regions are successfully avoided. See the Supplementary Information for more
 585 details on the development of the presented method and rejected alternatives.

586 In simulations the density within the identified regions throughout the simulation
 587 is within 0.15 /cc of the initial value for the NIMF case and 0.25 /cc of the initial value
 588 for the PSIMF case. Thus our method of isolating the pure magnetosheath and mag-
 589 netosphere is reliable and robust even for late stage KHI with roll-over and mixing.

590 When comparing the results of the simulation and the observation, we see good agree-
 591 ment for the growth rate for the NIMF and PSIMF case. GR from the NIMF simula-
 592 tion was within 5 km/s of the observational case for $\approx 20\%$ of the simulation, and the
 593 PSIMF case was in agreement for nearly 60% of the simulation.

594 • Plasma parameters from the automatically isolated regions were used to calculate
 595 KHI GR, UGR, and USA for the 45 KHI events in our database.

596 GR, UGR normalized to the local fast mode speed, and USA for the 45 KHI events
 597 in our database are reported in Table 2.

598 Growth rates range from a minimum of 3.93 to 103.16 km/s. When normalized to
 599 the fast mode speed, the unitless growth rate ranges from 0.005 to 0.325 in the extremes,
 600 with most events in the 0.01 to 0.20 range. That is, most of the observed KHI grow at
 601 a speed that is between 1% and 20% of the local fast mode speed.

602 Two of the events have unstable solid angles less than 1% of the total 4π solid an-
 603 gle. Unstable solid angles are between 1% and 10% for 23 events, and between 10% and
 604 25% for 17 events. Three events have unstable solid angles greater than 25% of the to-
 605 tal 4π solid angle. Larger solid angles are more common further down tail where the ve-

606 locity shear from the magnetosheath to the magnetosphere is greater and thus the sta-
 607 bilizing effects of the magnetic field are less influential.

608 We note a few of the observed events occur in apparently stable regions with very
 609 low growth rates (e.g: the high-latitude case on 25 Feb 2016 [*Nykyri et al.*, 2021; *Michael*
 610 *et al.*, 2021]); this does not preclude the observed events from being the KHI. Convec-
 611 tive instabilities, like the KHI, dissipate energy stored in unstable regions and systems.
 612 As excess energy is dissipated, the region becomes more stable, thus maximum instabil-
 613 ity and growth rates occur just prior to the formation of the instability. Because it is dif-
 614 ficult to identify the KHI in observational data until it is relatively well developed and
 615 has dissipated some of the excess free energy, observations will only be made after growth
 616 rates have decreased from their maxima. We believe those events occurring in apparently
 617 more stable regions may be later in development than faster growing KHI in less stable
 618 areas.

619 We also note the path MMS takes through the KHI event can have a significant
 620 effect on the growth rate determination. Encounters which merely skim the KH vortex
 621 rather than passing directly through it may actually grow faster than our calculations
 622 would indicate.

623

- The KHI is observed when SW flow speeds are between 295 and 610 km/s. Within
 624 this flow speed selection window, KHI GR, UGR, and USA are independent of pre-
 625 vailing SW conditions.

626 Values of the GR, UGR, and USA for each event are listed in Table 2. As can be
 627 seen in Figure 5, GR, UGR, and USA appear to be independent of SW conditions, with
 628 the exception of SW flow speed. All of the observed events occurred when the SW speed
 629 was between 295 and 610 km/s. At flow speeds much below 295 km/s the velocity shear
 630 is too low to satisfy the KHI onset conditions (Equation 1). At SW speeds above 610
 631 km/s the compressibility of the plasma will usually stabilize the KHI [*Miura and Pritch-
 632 ett*, 1982]. Within this selection window between 295 and 610 km/s however, flow speed
 633 is not correlated with GR, UGR, or USA. However, as can be seen in Figure 6, this se-
 634 lection window may merely reflect the distribution of SW speed throughout the entire
 635 4.5 year time range considered in this study.

636 The database of MMS KHI observations presented here will be used in future stud-
 637 ies of secondary processes associated with the KHI. The availability of burst mode data
 638 for all 45 events allows studies of secondary KHI processes to be extended to smaller spa-
 639 tial and temporal scales. The trends we have observed in the location and SW and IMF
 640 conditions may also be used to simplify the search for and identification of future KHI
 641 events.

642 **Acknowledgments**

643 Funding for this work was provided by the National Science Foundation under grant num-
 644 ber 1707521 and by NASA under grants numbers NNZ17AI50G and NNX16AF89G. Thanks
 645 are owed to the entire MMS team, and especially to the FGM and FPI instrument groups.
 646 MMS data was retrieved from the MMS Science Data Center at lasp.Colorado.edu/mms/sdc/public.
 647 OMNI solar wind data is available from NASA Goddard Space Flight Center's Space Physics
 648 Data Facility at omniweb.gsfc.nasa.gov.

649 **References**

650 Adamson, E., K. Nykyri, and A. Otto (2016), The Kelvin-Helmholtz instability un-
 651 der Parker-spiral interplanetary magnetic field conditions at the magnetosospheric
 652 flanks, *Advances in Space Research*, 58.

653 Axford, W., and C. Hines (1961), A unifying theory of high-Latitude phenomena
 654 and geomagnetic storms, *Canadian Journal of Physics*, 39, 1433–1464.

655 Birn, J. (1980), Computer studies of the dynamic evolution of the geomagnetic tail,
 656 *Journal of Geophysical Research*, 85, 1214–1222.

657 Burch, J. L., and T. D. Phan (2016), Magnetic reconnection and the dayside mag-
 658 netopause: advances with MMS, *Geophysical Research Letters*, 43, 8327–8338,
 659 doi:10.1002/2016GL069787.

660 Burch, J. L., T. E. Moore, R. B. Torbert, and B. L. Giles (2016), Magnetospheric
 661 Multiscale overview and science objectives, *Space Science Reviews*, 199, 5–21,
 662 doi:10.1007/s11214-015-0164-9.

663 Burkholder, B. L., K. Nykyri, X. Ma, R. Rice, S. A. Fuselier, K. J. Trattner, K. R.
 664 Pritchard, J. L. Burch, and S. M. Petrinec (2020), Magnetospheric multiscale ob-
 665 servation of an electron diffusion region at high latitudes, *Geophysical Research
 666 Letters*, 47(15), doi:10.1029/2020GL087268.

667 Chandrasekhar, S. (1961), *Hydrodynamic and Hydromagnetic Stability*, Oxford Uni-
668 versity Press.

669 Chaston, C. C., M. Wilber, M. Fujimoto, M. L. Goldstein, M. Acuna, H. Réme,
670 and A. Fazakerley (2007), Mode conversion of anomalous transport in Kelvin-
671 Helmholtz vortices and kinetic Alfvén waves at Earth's magnetopause, *Physical*
672 *Review Letters*, 99.

673 Dimmock, A. P., and K. Nykyri (2013), The statistical mapping of magnetosheath
674 plasma properties based on THEMIS measurements in the magnetosheath in-
675 terplanetary medium reference frame, *Journal of Geophysical Research*, 118,
676 4963–4876.

677 Dimmock, A. P., K. Nykyri, H. Karimabadi, A. Osmane, and T. I. Pulkkinen
678 (2015), A statistical study into the spatial distribution and dawn-dusk asym-
679 metry of dayside mangetosheath ion temperatures as a function of upstream
680 solar wind conditions, *Journal of Geophysical Research*, 120, 2767–2782, doi:
681 10.1002/2014JA020734.

682 Eriksson, S., B. Lavraud, F. D. Wilder, J. E. Stawarz, B. L. Giles, J. L. Burch,
683 W. Baumjohann, R. E. Ergun, P.-A. Lindqvist, W. Magnes, C. J. Pollock, C. R.
684 Russel, Y. Saito, R. J. Strangeway, R. B. Torbert, D. J. Gershmann, Y. V.
685 Khotyaintsev, J. C. Dorelli, S. J. Schwartz, L. Avanov, E. Grimes, Y. Vernisses,
686 A. P. Sturner, T. D. Phan, G. T. Marklund, T. E. Moore, W. R. Paterson, and
687 K. A. Goodrich (2016), Magnetospheric multiscale observations of magnetic recon-
688 nection associated with Kelvin-Helmholtz waves, *Geophysical Research Letters*, 43,
689 5606–5615, doi:10.1002/2016GL068783.

690 Fairfield, D. H., A. Otto, T. Mukai, S. Kokubun, R. P. Lepping, J. T. Steinberg,
691 A. J. Lazaurs, and T. Yamamoto (2000), Geotail observations of the Kelvin-
692 Helmholtz instability at the equatorial magnetotail boundary for parallel north-
693 ward fields, *Journal of Geophysical Research*, 105.

694 Foullon, C., C. J. Farrugia, A. N. Fazakerley, C. J. Owen, F. T. Gratton, and R. B.
695 Torbert (2008), Evolution of Kelvin-Helmholtz activity on the dusk flank magne-
696 topause, *Journal of Geophysical Research*, 113, doi:10.1029/2008JA013175.

697 Gosling, J. T., M. F. Thomsen, S. J. Bame, and C. T. Russell (1986), Accelerated
698 plasma flows at the near-tail magnetopause, *Journal of Geophysical Research:*
699 *Space Physics*, 91, doi:10.1029/JA091iA03p03029.

700 Hasegawa, H., M. Fujimoto, K. Maezawa, Y. Saito, and T. Mukai (2003), Geotail
701 observation of the dayside outer boundary region: Interplanetary magnetic field
702 control and dawn-dusk asymmetry, *Journal of Geophysical Research*, 108, doi:
703 10.1029/2002JA009667.

704 Hasegawa, H., M. Fujimoto, T.-D. Phan, H. Réme, A. Balogh, M. W. Dunlop,
705 C. Hashimoto, and R. TanDokoro (2004), Transport of solar wind into Earth's
706 magnetosphere through rolled-up Kelvin-Helmholtz vortices, *Nature*, 430, 755–758.

707 Hasegawa, H., M. Fujimoto, K. Takagi, Y. Saito, T. Mukai, and H. Réme (2006),
708 Single-spacecraft detection of rolled-up Kelvin-Helmholtz vortices at the flank
709 magnetopause, *Journal of Geophysical Research*, 111, doi:10.1029/2006JA011728.

710 Hasegawa, H., A. Retinò, A. Vaivads, Y. Khotyaintsev, M. Andre, T. K. M. Naka-
711 mura, L.-L. Teh, B. U. O. Sonnerup, S. J. Schwartz, Y. Seki, M. Fujimoto,
712 Y. Saito, H. Reme, and P. Canu (2009), Kelvin-Helmholtz waves at the Earth's
713 magnetopause: multiscale development and associated reconnection, *Geophysical
714 Research Letters*, 114, doi:10.1029/2009JA014042.

715 Henry, Z. W., K. Nykyri, T. W. Moore, A. P. Dimmock, and X. Ma (2017), On the
716 dawn-dusk asymmetry of the Kelvin-Helmholtz instability between 2007 and 2013,
717 *Journal of Geophysical Research*, 122, 11,888–11,900, doi:10.1002/2017JA024548.

718 Hwang, K.-J., M. L. Goldstein, M. M. Kuznetsova, Y. Wang, A. F. Viñas, and
719 D. G. Sibeck (2012), The first in situ observation of kelvin-helmholtz waves at
720 high-latitude magnetopause during strongly downward interplanetary magnetic
721 field conditions, *Journal of Geophysical Research: Space Physics*, 117(A8), doi:
722 10.1029/2011JA017256.

723 Johnson, J. R., C. Z. Cheng, and P. Song (2001), Signatures of mode conversion and
724 kinetic Alfvén waves at the magnetopause, *Geophysical Research Letters*, 28.

725 Kavosi, S., and J. Reader (2015), Ubiquity of Kelvin-Helmholtz waves at the Earth's
726 magnetopause, *Nature Communications*.

727 King, J. H., and N. E. Papitashvili (2005), Solar wind spatial scales in and com-
728 parisons of hourly wind and ACE plasma and magnetic field data, *Journal of
729 Geophysical Research*, 110, doi:10.1029/2004JA010649.

730 Li, W., M. Andre, Y. V. Khotyaintsev, A. Vaivads, D. B. Graham, S. Toledo-
731 Redondo, C. Norgren, P. Henri, C. Wang, B. B. Tang, B. Lavraud, Y. Vernisse,
732 D. L. Turner, J. Burch, R. Torbet, W. Magnes, C. T. Russell, J. B. Blake,

733 B. Mauk, B. Giles, C. Pollock, J. Fennell, A. Jaynes, L. A. Avanov, J. C. Dorellie,
 734 D. J. Gershman, W. R. Paterson, Y. Saito, and R. J. Strangeway (2016), Kinetic
 735 evidence of magnetic reconnection due to Kelvin-Helmholtz waves, *Geophysical*
 736 *Research Letters*, *43*, 5635–5643, doi:10.1002/2016GL069192.

737 Lin, D., C. Wang, W. Li, B. Tang, X. Guo, and Z. Peng (2014), Properties of
 738 Kelvin-Helmholtz waves at the magnetopause under northward interplanetary
 739 magnetic field: statistical study, *Journal of Geophysical Research: Space Physics*,
 740 *119*, 7485–7494, doi:10.1002/2014JA020379.

741 Ma, X., A. Otto, and P. Delamere (2014a), Interaction of magnetic reconnection
 742 and Kelvin-Helmholtz modes for large magnetic shear: 1. Kelvin-Helmholtz
 743 trigger, *Journal of Geophysical Research: Space Physics*, *119*, 781–797, doi:
 744 10.1002/2013JA019224.

745 Ma, X., A. Otto, and P. Delamere (2014b), Interation of magnetic reconnection and
 746 Kelvin-Helmholtz modes for large magnetic shear: 2. reconnection trigger, *Journal*
 747 *of Geophysical Research: Space Physics*, *119*, 808–820, doi:10.1002/2013JA019225.

748 Ma, X., A. Otto, P. A. Delamere, and H. Zhang (2016), Interaction between recon-
 749 nection and Kelvin-Helmholtz at the high-latitude magnetopause, *Advances in*
 750 *Space Research*, *58*(2), 231–239.

751 Ma, X., P. Delamere, A. Otto, and B. Burkholder (2017), Plasma transport driven
 752 by the three-dimensional Kelvin-Helmholtz instability, *Journal of Geophysical*
 753 *Research: Space Physics*, *122*, 10,382–10,395, doi:10.1002/2017JA024394.

754 Ma, X., P. Delamere, K. Nykyri, B. Burkholder, D. Neupane, and R. Rice (2019),
 755 Comparison between fluid simulation with test particles and hybrid simulation for
 756 the Kelvin-Helmholtz instability, *Journal of Geophysical Research: Space Physics*,
 757 *124*, 6654–6668, doi:10.1029/2019JA026890.

758 Merkin, V. G., J. G. Lyon, and S. G. Claudepierre (2013), Kelvin-Helmholtz in-
 759 stability of the magnetospheric boundary in a three-dimensional global MHD
 760 simulation during northward IMF conditions, *Journal of Geophysical Research:*
 761 *Space Physics*, *118*, 5478–5496, doi:10.1002/jgra.50520.

762 Michael, A. T., K. A. Sorathia, V. G. Merkin, K. Nykyri, B. L. Burkholder, X. Ma,
 763 A. Y. Ukhorskiy, and J. Garretson (2021), Modeling Kelvin-Helmholtz Instabil-
 764 ity at the High-Latitude Boundary Layer in a Global Magnetosphere Simulation,
 765 *Geophysical Research Letters*, *48*(19), doi:10.1029/2021GL094002.

766 Miura, A. (1984), Anomalous transport by magnetohydrodynamic Kelvin-Helmholtz
767 instabilities in the solar wind-magnetosphere interaction, *Journal of Geophysical*
768 *Research*, 89, 801–818.

769 Miura, A. (1987), Simulation of the Kelvin-Helmholtz instability at the magneto-
770 spheric boundary, *Journal of Geophysical Research*, 92, 3195–3206.

771 Miura, A., and P. L. Pritchett (1982), Nonlocal stability analysis of the MHD
772 Kelvin-Helmholtz instability in a compressible plasma, *Journal of Geophysical*
773 *Research*, 87, 7431–7444.

774 Moore, T. W., K. Nykyri, and A. P. Dimmock (2016), Cross-scale energy transport
775 in space plasmas, *Nature Physics*.

776 Moore, T. W., K. Nykyri, and A. P. Dimmock (2017), Ion-scale wave properties
777 and enhanced ion heating across the low-latitude boundary layer during Kelvin-
778 Helmholtz instability, *Journal of Geophysical Research: Space Physics*, 122,
779 11,128–11,153, doi:10.1002/2017JA024591.

780 Nykyri, K. (2013), Impact of MHD shock physics on magnetosheath asymmetry and
781 Kelvin-Helmholtz instability, *Journal of Geophysical Research: Space Physics*, 118,
782 5068–5081.

783 Nykyri, K., and A. Otto (2001), Plasma transport at the magnetopause boundary
784 due to reconnection in Kelvin-Helmholtz vortices, *Geophysical Research Letters*,
785 28, 3565–3568.

786 Nykyri, K., and A. Otto (2004), Influence of the Hall term on KH instability and
787 reconnection inside KH vortices, *Annales Geophysicae*, 22, 935–949.

788 Nykyri, K., A. Otto, J. Büchner, B. Nikutowski, W. Baumjohann, L. M. Kistler,
789 and C. Mouikis (2003), Equator-S observations of boundary signatures: FTE's
790 or Kelvin-Helmholtz waves?, in *Earth's Low-Latitude Boundary Layer*, *Geophysical Monograph*, vol. 133, edited by P. T. Newell and R. Onsager, pp. 205–210,
791 American Geophysical Union.

792 Nykyri, K., A. Otto, B. Lavraud, C. Mouikis, L. M. Kistler, A. Balogh, and
793 H. Réme (2006), Cluster observations of reconnection due to the Kelvin-Helmholtz
794 instability at the dawnside magnetospheric flank, *Annales Geophysicae*, 24, 2619–
795 2643.

796 Nykyri, K., A. Otto, E. Adamson, and J. Mumme (2011a), Cluster observations of
797 a cusp diamagnetic cavity: structure, size, and dynamics, *Journal of Geophysical*

799 *Research*, 116, doi:10.1029/2010JA015897.

800 Nykyri, K., A. Otto, E. Adamson, and A. Tjulin (2011b), On the origin of fluc-
801 tuation in the cusp diamagnetic cavity, *Journal of Geophysical Research*, 116,
802 doi:10.1029/2010JA015888.

803 Nykyri, K., X. Ma, A. Dimmock, C. Foullon, A. Otto, and A. Osmane (2017), In-
804 fluence of velocity fluctuations on the Kelvin-Helmholtz instability and its as-
805 sociated mass transport, *Journal of Geophysical Research*, 122, 9489–9512, doi:
806 10.1002/2017JA024374.

807 Nykyri, K., X. Ma, B. Burkholder, R. Rice, J. R. Johnson, E.-K. Kim, P. Delamere,
808 A. Michael, K. Sorathia, D. Lin, S. Merkin, S. Fuselier, J. Broll, O. Le Contel,
809 D. Gershman, I. Cohen, B. Giles, R. J. Strangeway, C. T. Russell, and J. L. Burch
810 (2021), MMS observations of the multiscale wave structures and parallel elec-
811 tron heating in the vicinity of the southern exterior cusp, *Journal of Geophysical
812 Research: Space Physics*, 126(3), doi:10.1029/2019JA027698.

813 Otto, A. (1990), 3D resistive MHD computations of magnetospheric physics, *Com-
814 puter Physics Communications*, 59, 185–195.

815 Otto, A., and D. H. Fairfield (2000), Kelvin-Helmholtz instability at the magnetotail
816 boundary: MHD simulation and comparison with Geotail observations, *Journal of
817 Geophysical Research*, 105, 21,175–21,190.

818 Paschmann, G., B. U. Ö. Sonnerup, I. Papamastorakis, G. Haerendel, S. J. Bame,
819 J. R. Asbridge, J. T. Gosling, C. T. Russell, and R. C. Elphic (1979), Plasma
820 acceleration at the Earth’s magnetopause: evidence for reconnection, *Nature*, 282,
821 243–246.

822 Pollock, C., T. Moore, A. Jacques, J. Burch, U. Gliese, Y. Saito, T. Omoto,
823 L. Avanov, A. Barrie, V. Coffey, J. Dorelli, D. Gershman, B. Giles, T. Ros-
824 nack, C. Salo, S. Yokota, M. Adrian, C. Aoustin, C. Auletti, S. Aung, V. Bigio,
825 N. Cao, M. Chandler, D. Chornay, K. Christian, G. Clark, G. Collinson, T. Cor-
826 ris, A. D. L. Santos, R. Devlin, T. Diaz, T. Dickerson, C. Dickson, A. Diekmann,
827 F. Diggs, C. Duncan, A. Figueroa-Vinas, C. Firman, M. Freeman, N. Galassi,
828 K. Garcia, G. Goodhart, D. Guererro, J. Hageman, J. Hanley, E. Hemminger,
829 M. Holland, M. Hutchins, T. James, W. Jones, S. Kreisler, J. Kujawaski, V. Lavu,
830 J. Lobell, E. LeCompte, A. Lukemire, E. MacDonald, A. Mariano, T. Mukai,
831 K. Narayanan, Q. Nguyen, M. Onizuka, W. Paterson, S. Persyn, B. Piepgrass,

832 F. Cheey, A. Rager, T. Raghuram, A. Ramil, L. Reichenthal, H. Rodriguez,
 833 J. Rouzaud, A. Rucker, Y. Saito, M. Samara, J.-A. Sauvaud, D. Schuster,
 834 M. Shappirio, K. Shelton, D. Sher, D. Smith, K. Smith, S. Smith, D. Steinfeld,
 835 R. Szymkiewicz, K. Tanimoto, J. Taylor, C. Tucker, K. Tull, A. Uhl, J. Vloet,
 836 P. Walpole, S. Weidner, D. White, G. Winkert, P.-S. Yeh, and M. Zeuch (2016),
 837 Fast plasma investigation for Magnetospheric Multiscale, *Space Science Reviews*,
 838 199, 331–406, doi:10.1007/s11214-016-0245-4.

839 Potter, D. (1973), *Computational Physics*, John Wiley and Sons.

840 Russell, C. T., B. J. Anderson, W. Baumjohann, K. R. Bromund, D. Dearborn,
 841 D. Fischer, G. Le, H. K. Leinweber, D. Lenema, W. Magnes, J. D. Means, M. B.
 842 Moldwin, R. Nakamura, D. Pierce, F. Plaschke, K. M. Rowe, J. A. Slavin, R. J.
 843 Strangeway, R. Torbert, C. Hagen, I. Jernej, A. Valavanoglou, and I. Ricter (2016),
 844 The Magnetospheric Multiscale magnetometers, *Space Science Reviews*, 199, 189–
 845 256, doi:10.1007/s11214-014-0057-3.

846 Sonnerup, B. U. Ö., and M. Scheible (1998), *Analysis Methods for Multi-Spacecraft*
 847 *Data*, chap. Minimum and Maximum Variance Analysis, pp. 185–220, Interna-
 848 tional Space Science Institute.

849 Sonnerup, B. U. Ö., G. Paschmann, I. Papamastorakis, N. Sckopke, G. Haerendel,
 850 S. J. Bame, J. R. Asbridge, J. T. Gosling, and C. T. Russell (1981), Evidence for
 851 magnetic field reconnection at the Earth’s magnetopause, *Journal of Geophysical*
 852 *Research: Space Physics*, 86, doi:10.1029/JA086iA12p10049.

853 Sorathia, K. A., V. G. Merkin, A. Y. Ukhorskiy, R. C. Allen, K. Nykyri,
 854 and S. Wing (2019), Solar wind ion entry into the magnetosphere during
 855 northward IMF, *Journal of Geophysical Research: Space Physics*, 124, doi:
 856 doi.org/10.1029/2019JA026728.

857 Stawarz, J. E., S. Eriksson, F. D. Wilder, R. E. Ergun, S. J. Schwartz, A. Pou-
 858 quet, J. L. Burch, B. L. Giles, Y. Khotyaintsev, O. L. Contel, P.-A. Lindqvist,
 859 W. Magnes, C. J. Pollock, C. T. Russll, R. J. Strangeway, R. B. Torbert, L. A.
 860 Avanov, J. C. Dorelli, J. P. Eastwood, D. J. Gershman, K. A. Goodrich, D. M.
 861 Malaspina, G. T. Marklund, L. Mirioni, and A. P. Sturner (2016), Observations
 862 of turbulence in a Kelvin-Helmholtz event on 8 September 2015 by the Magneto-
 863 spheric Multiscale mission, *Journal of Geophysical Research*, 121, 11,021–11,034,
 864 doi:10.1002/10JA023458.

865 Taylor, M. G. G. T., B. Lavraud, C. P. Escoubet, S. E. Milan, K. Nykyri, M. W.
866 Dunlop, J. A. Davies, R. H. W. Friedel, H. Frey, Y. V. Bogdanova, A. Asnes,
867 H. Laasko, P. Trvincek, A. Masson, H. Opgenoorth, C. Vallat, A. N. Fazaker-
868 ley, A. D. Lahiff, C. J. Owen, F. Pitout, Z. Pu, C. Shen, Q. G. Zong, H. Rme,
869 J. Scudder, and T. L. Zhang (2008), The plasma sheet and boundary layers un-
870 der northward IMF: a multi-point and multi-instrument perspective, *Advances in*
871 *Space Research*, *41*, 1619–1629.

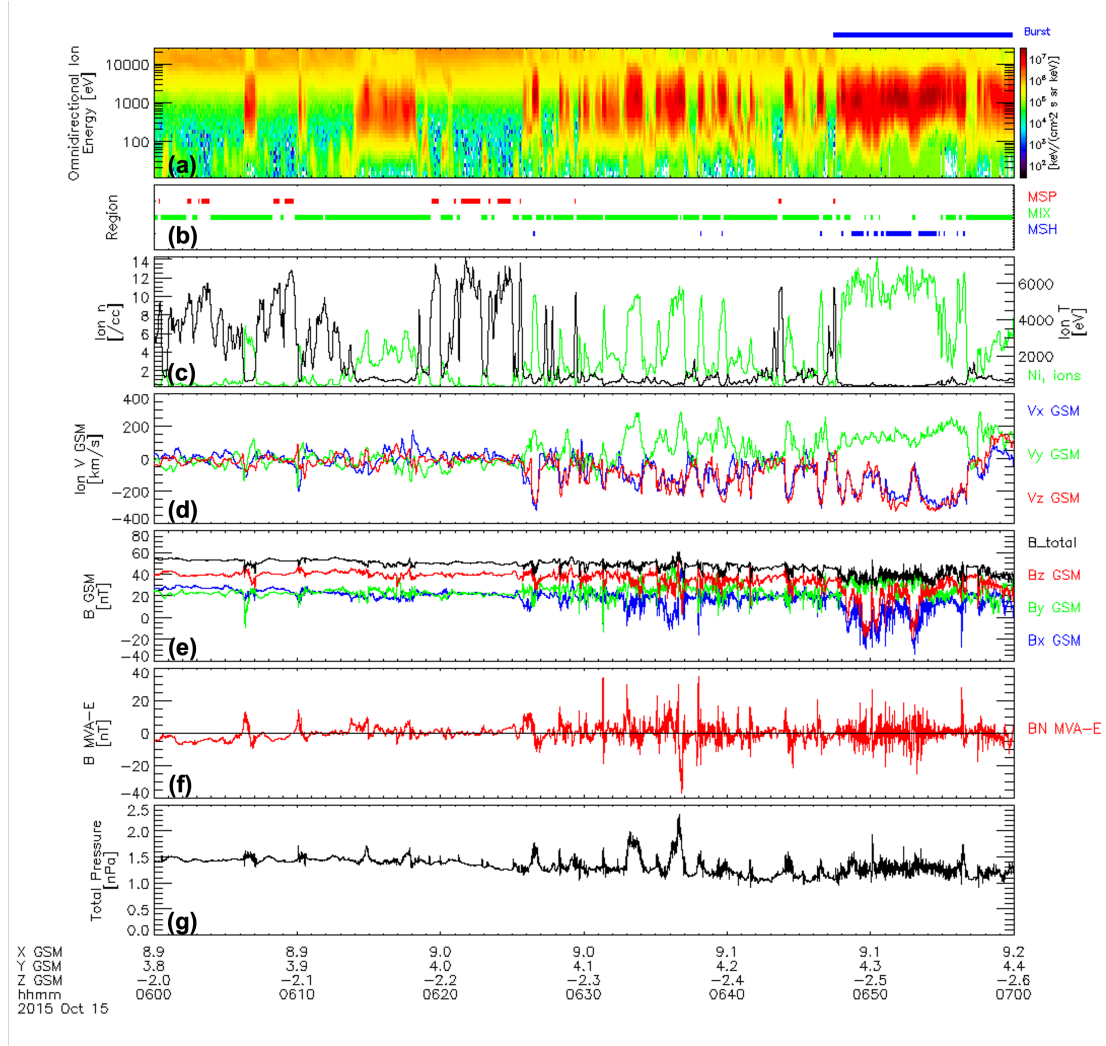
872 Taylor, M. G. G. T., H. Hasegawa, B. Lavraud, T. Phan, C. P. Escobet, M. W.
873 Dunlop, Y. V. Bogdanova, A. L. Borg, M. Volwerk, J. Berchem, O. D. Constan-
874 tinescu, J. P. Eastwood, A. Masson, H. Laakso, J. Soucek, A. N. Fazakerley,
875 H. Frey, E. V. Panov, C. Shen, J. K. Shi, D. G. Sibeck, Z. Y. Pu, J. Wang, and
876 J. A. Wild (2012), Spatial distribution of rolled up Kelvin-Helmholtz vortices at
877 Earth’s dayside and flank magnetopause, *Annales Geophysicae*, *30*, 1025–1035,
878 doi:10.5194/angeo-30-1025-2012.

879 Torbert, R. B., C. T. Russell, w. Magnes, R. E. Ergun, P.-A. Lindqvist, O. LeCon-
880 tel, H. Vaith, J. Macri, S. Myers, D. Rau, J. Needell, B. King, M. Granoff,
881 M. Chutter, I. Dors, G. Olsson, Y. V. Khotyaintsev, A. Eriksson, C. A. Klet-
882 zing, S. Bounds, B. Anderson, W. Baumjohann, M. Steller, K. Bromund,
883 G. Le, R. Nakamura, R. J. Strangeway, H. K. Leinweber, S. Tucker, J. West-
884 fell, D. Fisher, F. Plaschke, J. Porter, and K. Lappalainen (2016), The FIELDS
885 instrument suite on MMS: scientific objectives, measurements, and data products,
886 *Space Science Reviews*, *199*, 105–135, doi:10.1007/s11214=014-0109-8.

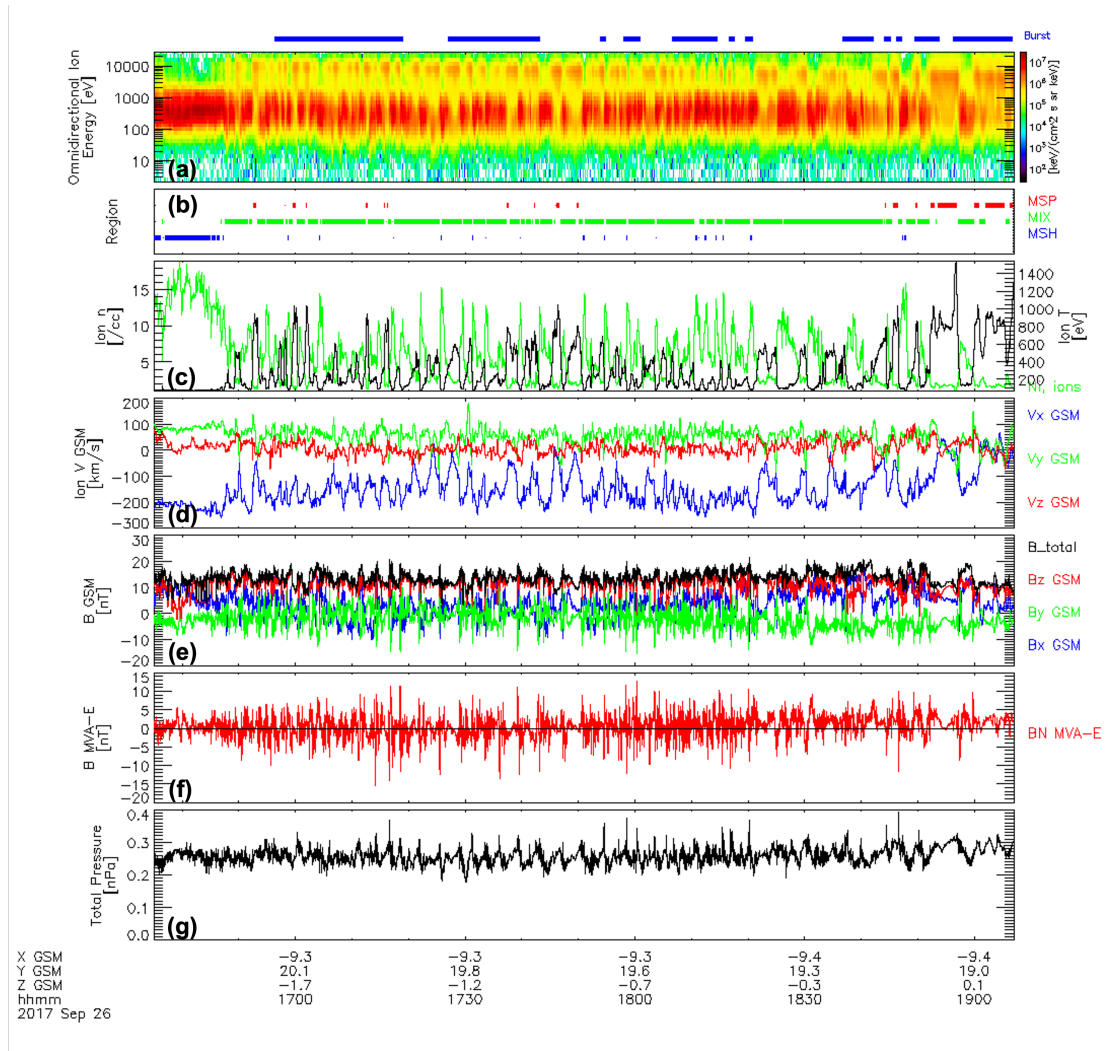
887 Wilder, F. D., R. E. Ergun, S. J. Schwartz, D. L. Newman, S. Eriksson, J. E.
888 Stawarz, M. V. Goldman, K. A. Goodrich, D. J. Gershman, D. M. Malaspina,
889 J. C. Holmes, A. P. Sturner, J. L. Burch, R. B. Torbert, P.-A. Lindqvist, G. T.
890 Marklund, Y. Khotyaintsev, R. J. Strangeway, C. T. Russel, C. J. Pollock, B. L.
891 Giles, J. C. Dorelli, L. A. Avanov, W. R. Patterson, F. Plaschke, and W. Magnes
892 (2016), Observations of large-amplitude, parallel, electrostatic waves associated
893 with the Kelvin-Helmholtz instability by the Magnetospheric Multiscale mission,
894 *Geophysical Research Letters*, *43*, 8859–8866, doi:10.1002/2016GL070404.

895 Wing, S., J. R. Johnson, P. T. Newell, and C.-I. Meng (2005), Dawn-dusk asym-
896 metries, ion spectra, and sources in the northward interplanetary magnetic field
897 plasma sheet, *Journal of Geophysical Research*, *110*, doi:10.1029//2005JA011086.

898 Zhao, C., C. T. Russell, R. J. Strangeway, S. M. Petrinec, W. R. Paterson, M. Zhou,
899 B. J. Anderson, W. Baumjohann, K. R. Bromund, M. Chutter, D. Fischer,
900 G. Le, R. Nakamura, F. Plaschke, J. A. Slavin, R. B. Torbert, and H. Y. Wei
901 (2016), Force balance at the magnetopause determined with MMS: application
902 to flux transfer events, *Geophysical Research Letters*, *43*, 11,941–11,947, doi:
903 10.1002/2016GL071568.



211 **Figure 1.** MMS observations of (a) omnidirectional ion energies; (b) plasma region; (c) ion
 212 density (green) and temperature (black); (d) ion bulk velocity in GSM coordinates; (e) direct
 213 current magnetic field in GSM coordinates; (f) the normal component of the magnetic field; and
 214 (g) total pressure from 06:00 to 07:00 UT on 15 October 2015. Ion data is taken from the Fast
 215 Plasma Investigation (FPI) and magnetic field data is from the Flux Gate Magnetometer (FGM)
 216 aboard MMS1. Burst mode data is available for the intervals marked in blue above the panels.



228

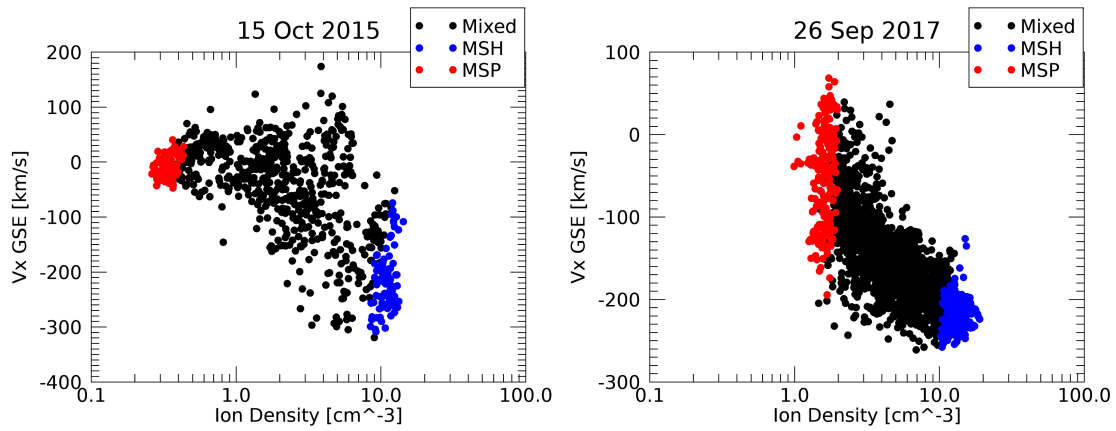
Figure 2. MMS observations as in Figure 1 from 16:35 to 19:07 UT on 26 September 2017.

229

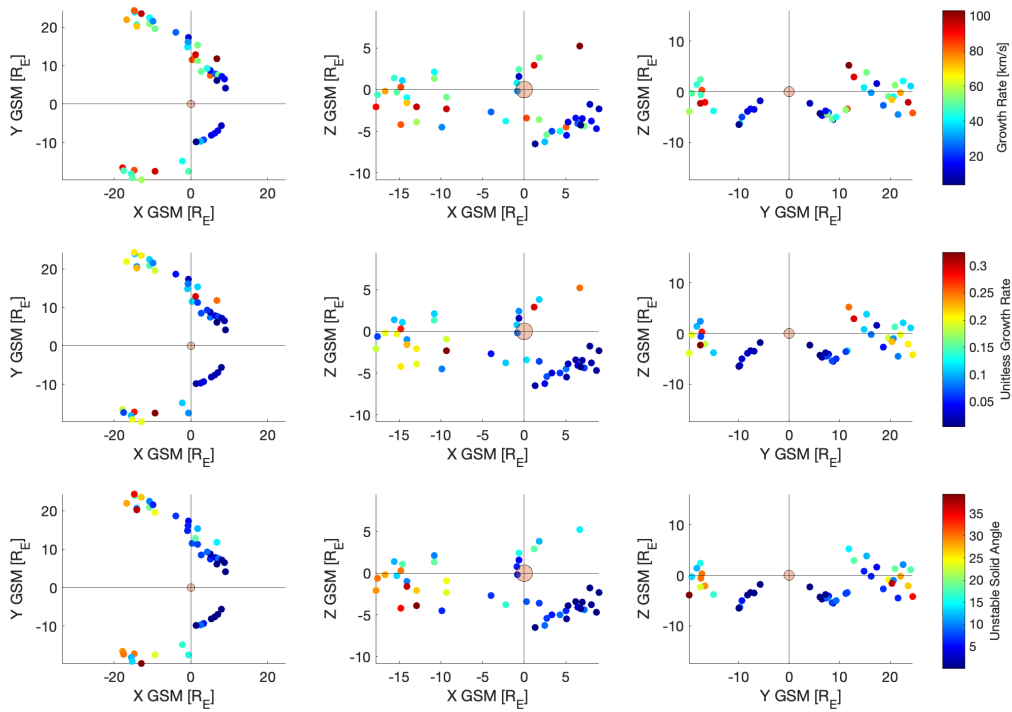
Ion data is taken from the Fast Plasma Investigation (FPI) and magnetic field data is from the Flux Gate Magnetometer (FGM) aboard MMS1. Burst mode data is available for the intervals marked in blue at top.

230

231



324 **Figure 3.** MMS observations of tailward ion velocity as a function of ion density for 06:00-
 325 07:00 on 15 October 2015 (left) and 16:35-19:07 on 26 September 2017. Blue (red) points were
 326 identified as magnetosheath (magnetospheric) plasma. Mixed and ambiguous regions are plotted
 327 in black. For the 2017 example event, ions show clear evidence of roll-over within the KHI vor-
 328 tex, low density plasma typically associated with the magnetosphere is moving tailward with the
 329 faster magnetosheath plasma, but this is not seen for the 2015 example event. The overall shape
 330 of both events however, is consistent with previous studies of the KHI.



426 **Figure 4.** Growth rates (GR, top row), unitless growth rates (UGR, middle row), and un-
 427 stable solid angles (USA, bottom row) plotted with respect to the KHI's location along the
 428 magnetopause in GSM X-Y plane (left column), X-Z plane (middle column), and Y-Z plane
 429 (right column).

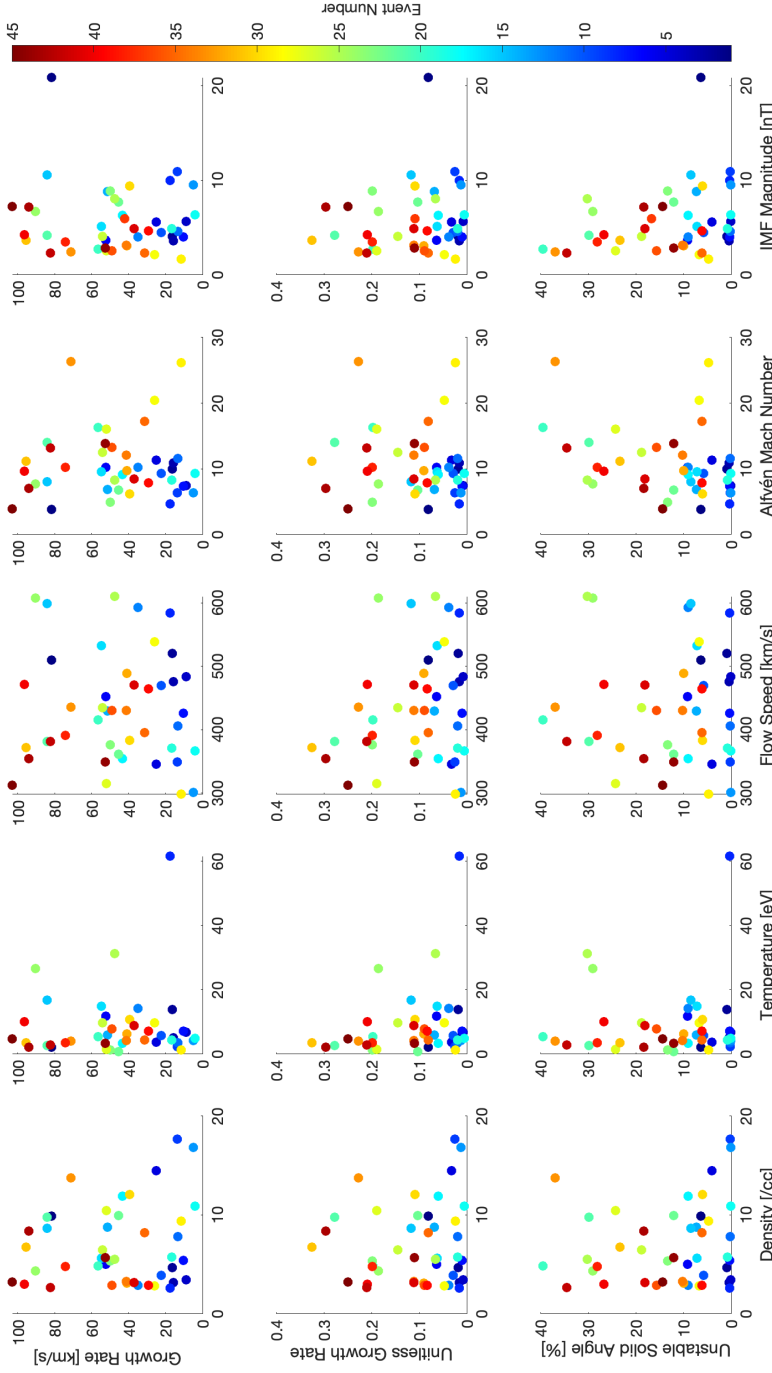
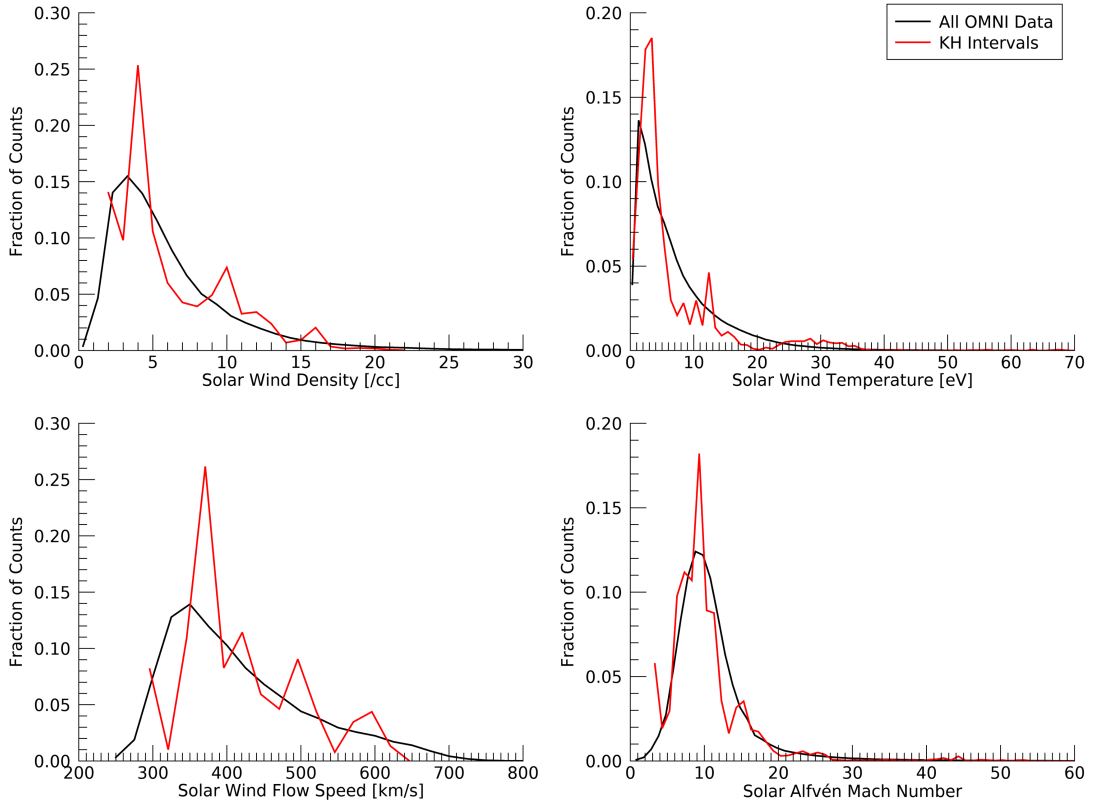
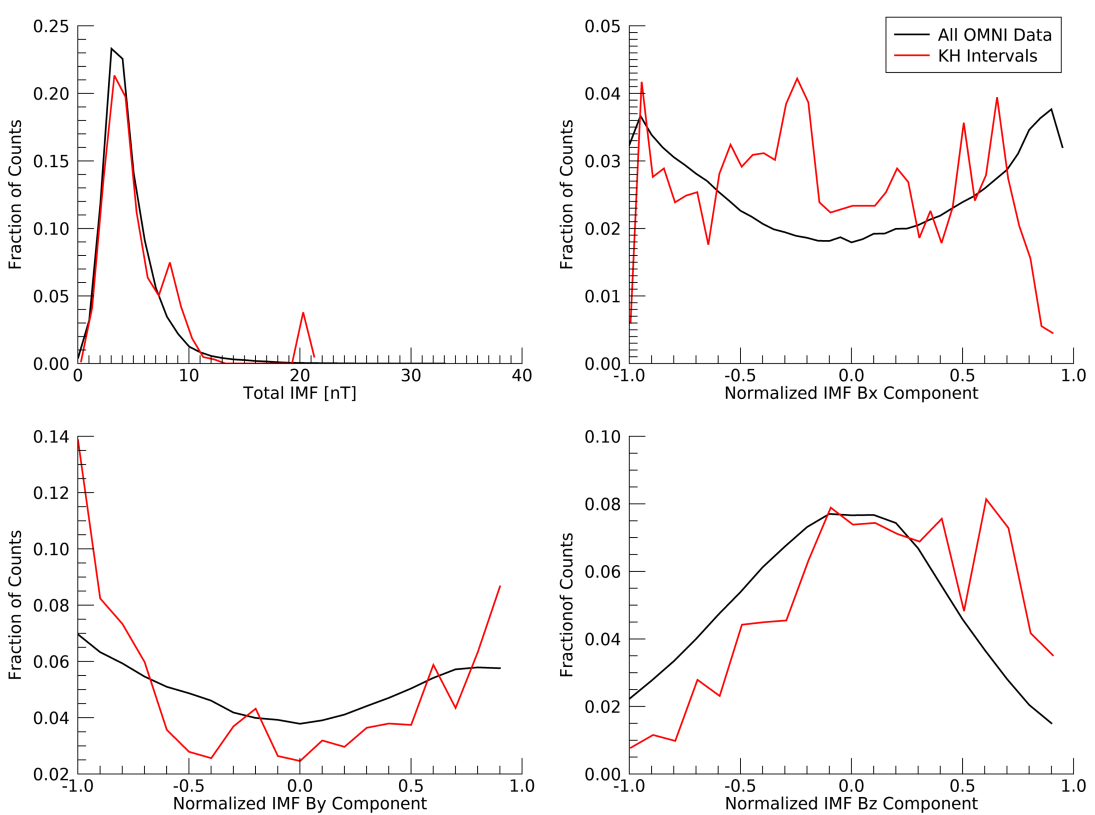


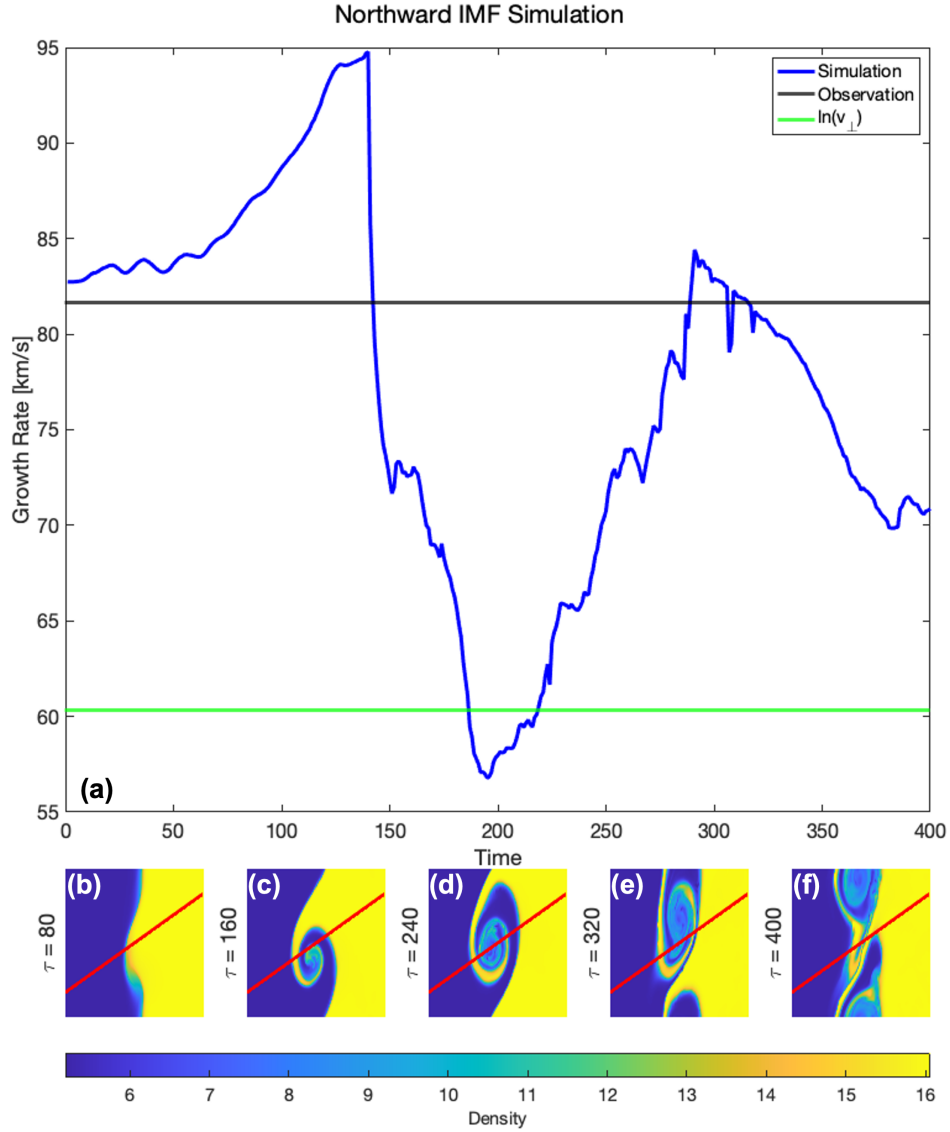
Figure 5. KHI growth rates (GR, top), unitless growth rates (UGR, middle), and unstable solid angles (USA, bottom) as a function of SW density (far left), temperature (center left), flow speed (center), Alfvén mach number (center right), and average IMF magnitude (far right). Other than a selection window from 295-610 km/s flow speed, GR, UGR, and USA are independent of solar wind parameters. The color bar indicates each unique event for comparison from plot to plot.



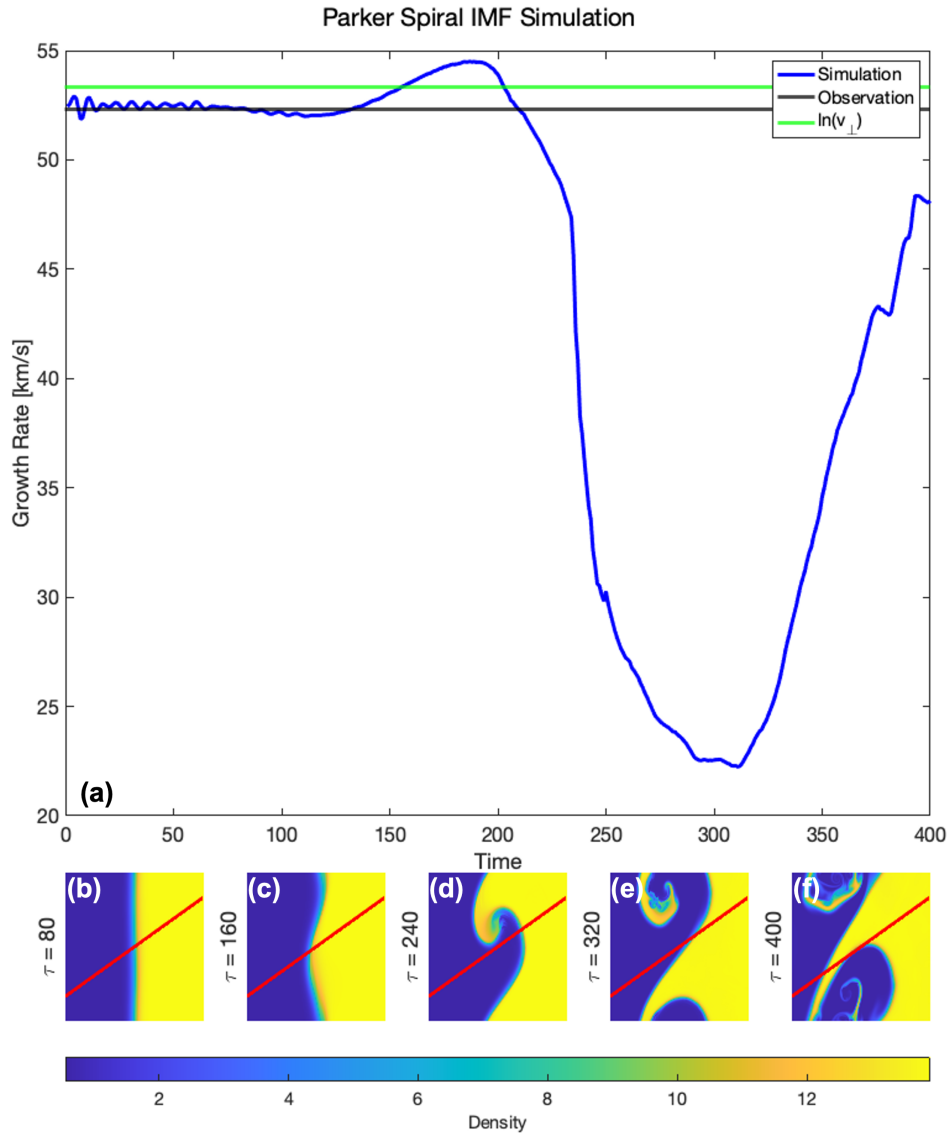
479 **Figure 6.** Normalized histograms of solar wind density (top left), temperature (top right),
 480 speed (bottom left), and Alfvén Mach number (bottom right) for the complete time range con-
 481 sidered in this study, 01 September 2015 to 31 March 2020 (black), and for the intervals during
 482 which MMS observed the KHI (red).



491 **Figure 7.** Normalized histograms of IMF magnitude (top left) and normalized IMF compo-
 492 nents for the complete time range considered in this study, 01 September 2015 to 31 March 2020
 493 (black), and for the intervals during which MMS observed the KHI (red).



525 **Figure 8.** Growth rates were calculated and plotted as a function of time (a) using data from
 526 2D MHD simulations of a dusk flank KHI occurring during Northward IMF. Initial conditions
 527 of the simulation are based on the event MMS observed on 08 September 2015. Black and green
 528 lines indicate the GR for the MMS event on which the simulation is based and the simulation GR
 529 as described in Section 4, respectively. Density data from several time steps within the simula-
 530 tion (b)-(f) show the development of the KHI. Cuts (red lines (b)-(f)), were taken through the
 531 instability at every simulation time step.



532 **Figure 9.** The KHI growth rates as in Figure 8 for a 2D MHD simulation of a dusk flank KHI
 533 occurring during Parker Spiral IMF orientation. Initial conditions of the simulation are based on
 534 the event MMS observed on 18 October 2015.